This document was prepared for the ETI by third parties under contract to the ETI. The ETI is making these documents and data available to the public to inform the debate on low carbon energy innovation and deployment.

Programme Area: Marine

Project: PerAWAT

Title: Report on Model Setup for Ducted Horizontal-Axis Axial Flow Turbines

Abstract:

This report details simulations of a three-bladed axial flow ducted tidal turbine. Additionally, the report describes fundamental work carried out to enable these blade-resolved simulations, including duct design and rotor modelling.

Context:

The Performance Assessment of Wave and Tidal Array Systems (PerAWaT) project, launched in October 2009 with £8m of ETI investment. The project delivered validated, commercial software tools capable of significantly reducing the levels of uncertainty associated with predicting the energy yield of major wave and tidal stream energy arrays. It also produced information that will help reduce commercial risk of future large scale wave and tidal array developments.

Energy Technologies Institute

PerAWaT

WG3 WP1 D2: REPORT ON MODEL SETUP FOR DUCTED HORIZONTAL-AXIS AXIAL FLOW TURBINES

Authors C. Fleming, S. C. McIntosh, R.H.J. Willden

Version 2.0

Date 26/08/11

Revision History		
Issue / Version	**Issue Date**	**Summary**
0.1	23/05/11	First draft for review by GH
1.0	27/05/11	Updated draft following comments from GH
2.0	26/08/11	Updated following ETI review

Executive Summary

The report details simulations of a three-bladed axial flow ducted tidal turbine. Additionally, the report describes fundamental work carried out to enable these blade-resolved simulations, including duct design and rotor modelling.

The bi-directional duct is designed with the aid of a computational flow solver. The design process involves the simulation of a range of candidate geometries where camber and thickness are varied methodically, with the rotor modelled as an actuator disk. Device performance is assessed based on power, thrust and efficiency characteristics under fully turbulent flow conditions. Performance comparisons are made based on overall device dimensions rather than rotor area. The final duct combines desirable features of several candidate designs. The ability of the bi-directional turbines tested to increase both the mass-flow through and the pressure-drop across the rotor is limited. An unducted reference case, of the same outer dimensions, yields a power coefficient 75% greater than that of the best bi-directional ducted design tested.

The selected duct is then modelled incorporating the University of Manchester's 1/70th scale rotor, operating in the 1m deep EDF flume. We conduct two levels of numerical modelling; fully blade-resolved simulations and a novel Blade Element Momentum (BEM) theory Computational Fluid Dynamics (CFD) embedded model. We find favourable agreement between the two models. Further we note that the Manchester rotor was designed for unducted operation, and use the BEM embedded model to design a bespoke rotor for operation in the ducted environment.

The three-dimensional, blade-resolved computational model of the ducted turbine shows excellent agreement with the embedded BEM predictions. One pertinent feature of ducted turbine flows is that the helical tip-vortex structure, readily identifiable in unducted rotor wakes, is not discernible. This is attributed to a bounding effect of the inner duct wall. For ducted turbines bound circulation is largely maintained to the blade tip, thus limiting the production of a tip vortex. A cylindrical vortex sheet is generated emanating from the downstream edge of the duct to account for the momentum loss in the rotor wake.

Table of contents

1 Introduction

This report forms deliverable D2 of Work Group 3 Work Package 1 of the PerAWaT project. The work in this deliverable, carried out at the University of Oxford, involves numerical simulation of ducted axial-flow tidal turbines at model scale. Model validity, as well as capability to replicate complementary experimental work, are demonstrated. The report describes model structure and functioning, including all assumptions and algorithms.

This body of work is presented in three sections, covering details of work carried out on duct design (Section 2), rotor modelling (Section 3) and device simulation (Section 4) respectively.

At the outset of this project it was anticipated that a ducted turbine would be available for experimental testing and complementary numerical simulation. However, the consortium was unable to source a suitable ducted turbine from between themselves and their contacts. Hence, the consortium took a decision to design, build and test a suitable ducted turbine with several consortium partners involved as follows; supply of rotor and drive train from $1/70^{th}$ scale model testing (Manchester), hydrodynamic design of duct (Oxford), support structure and construction (Garrad Hassan), testing at EDF flume. This work naturally falls outside of all current deliverables but will be included within a future contract variation relating to reprofiling of the experimental testing programme. The hydrodynamic design of the ducted turbine forms a natural prerequisite to the demonstration of validity of the ducted turbine simulation model which was the intended sole subject of this deliverable. Hence, Oxford's contribution to the hydrodynamic design of the ducted turbine is included here also.

The consortium have chosen to base the ducted device design around a 27 *cm* rotor, previously designed for array-scale testing at the University of Manchester, for testing within the experimental facility at EDF in Paris. The hydrodynamic design of the duct is included in this report in Section 2. Details of the methods used, including design considerations, performance metrics, and computational setup are given in Section 2.1. A series of candidate designs are

compared based on power generation, thrust loading and efficiency in Section 2.2, and the best-performing bi-directional duct is selected.

It is clear that rotors designed and optimized for operation in unconfined flow environments will not in general be optimal for operation in the presence of other bodies; e.g. flow constraints presented by flume walls, floor and free surface, or ducting surrounding the rotor itself. Whilst the Blade Element Momentum (BEM) method widely used in the wind industry forms a reliable design tool for unducted flows, as well as a source of comparative data for unducted turbine simulations as presented in WG3 WP1 D1, its use for such purposes for ducted turbines is questionable. To account for blockage and duct proximity we develop and use a hybrid BEM-RANS (Reynolds Averaged Navier-Stokes) method in Section 3.1. The method comprises BEM, resolving rotor operation within a thin disk region, embedded within a three-dimensional RANS solver to simulate the surrounding flow field. A further enhancement to the method (Section 3.2) enables a rotor to be optimized, within constraints, for a given flow environment, e.g. operation within a duct. Comparisons are made between devices featuring generic and bespoke rotor designs.

In Section 4, a series of three-dimensional RANS simulations are presented. These simulations, featuring explicit geometric reproduction of the rotor geometry, are referred to as "blade-resolved" simulations. Boundary conditions and turbulence parameters for the flume environment have previously been developed in WG3 WP1 D1 and are applied again here. A grid resolution study (Section 4.2.1) is conducted to determine appropriate mesh topology at the rotor. Further details of the computational setup are given in Section 4.3, which is followed by a discussion of the results. In lieu of any reliable experimental data for ducted turbines the accuracy of the blade-resolved simulations is gauged by comparison to predictions by the RANS-embedded BEM method.

2 Duct Design

Many tidal energy converters currently in development feature a ducted rotor (Clean Current 2011, Open Hydro 2011). Significant performance improvements for ducted devices over unducted devices have been reported both by developers and researchers (Grassman 2003). One goal of the PerAWaT project is to improve understanding of ducted axial-flow turbines, through experimental and computational modelling. During the planning stages of the project, it was envisaged that such modelling would be carried out on an existing device design, which would be sourced from a commercial developer. This has not proved possible so a suitable ducted device must be designed anew from within the consortium. The authors have taken responsibility for the hydrodynamic design of the duct, which is reported in this deliverable in addition to the original requirements of the deliverable.

2.1 Methods

In this work the mechanisms by which the duct increases velocity at the rotor plane are investigated. A series of candidate duct designs (denoted A to G), with wide variations in duct curvature and thickness are produced and simulated. For comparative purposes, an unducted device and a commercial ducted device (Clean Current 2011) are also modelled. Duct parameters that lead to desirable performance characteristics are identified, and incorporated into subsequent design iterations. Simulations are conducted within the flow environment of the EDF flume, width 1.5 *m*, depth 1 *m* and flow speed 0.27 *m/s*, which is the flume in which it is intended to test the ducted turbine developed.

The focus of the current simulations is on the relative performance of a series of ducted tidal turbines. The streamwise thrusts of the duct and rotor respectively have a large influence on device performance. Tangential and radial components of flow, associated with real rotors, are not expected to affect relative performance and hence may be disregarded. These conditions are met appropriately by a porous disk model of the rotor. Details of how the appropriate streamwise thrust is applied are given in Section 2.1.2.

At low blockage ratios (~8% in this case), the change in free-surface height, associated with the removal of momentum from the flow, is small and has a negligible effect on device performance (Consul *et al*, 2011). For the duct-design simulations, the free-surface is modelled as a rigid lid, thus avoiding the computational overhead associated with free-surface tracking methods.

2.1.1 Design Considerations

Conventionally, in comparisons between ducted and unducted devices, the rotor diameter is held constant (Hansen 2000, Crawford 2010). Consequently, it is unclear whether any resulting improvement in performance is due to acceleration of the flow by the duct, increased flow blockage or increased upstream capture width.

The available power within a streamtube is

$$P = \frac{1}{2}\rho A u^3 \quad \textbf{(1)}$$

where ρ is the fluid density, A the cross-sectional area of the streamtube, and u the free-stream velocity. The motivation for enclosing a rotor within a duct is to increase the flow velocity at the rotor, leading to an increase in available power.

To facilitate comparison between competing duct designs we choose to hold external blockage constant by using a constant maximum outer dimension of each duct of 0.4 m, while the rotor diameter is allowed to vary within the duct according to its internal surface curvature. The choice of 0.4 m originates from a desire to not overly block the flow or overly constrain external flow features (separations) that have been observed in previous studies of ducted turbines (Belloni & Willden 2010). A duct length-to-diameter ratio of 1:1 is used throughout, an aspect ratio that reflects observations of current commercial designs (Clean Current 2011). An appropriately scaled commercial design (AECOM 2009) and an unducted device of diameter 0.4 m are simulated for comparative purposes. Schematic diagrams of the test series are laid out in Figure 2.1.1. Ducts A to G were tested initially, and the results of those

simulations informed the design of duct H (cf. Section 2.2), which combines the internal surface of duct D with a flat external surface.

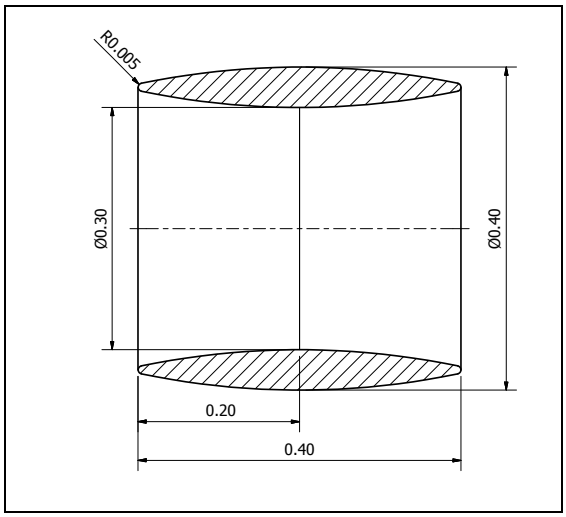

(A)

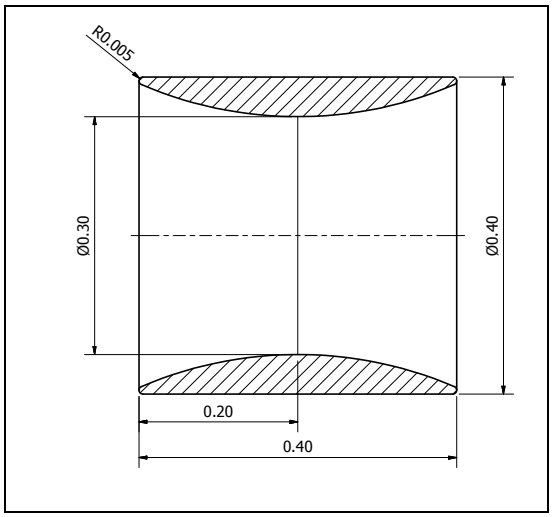

(B)

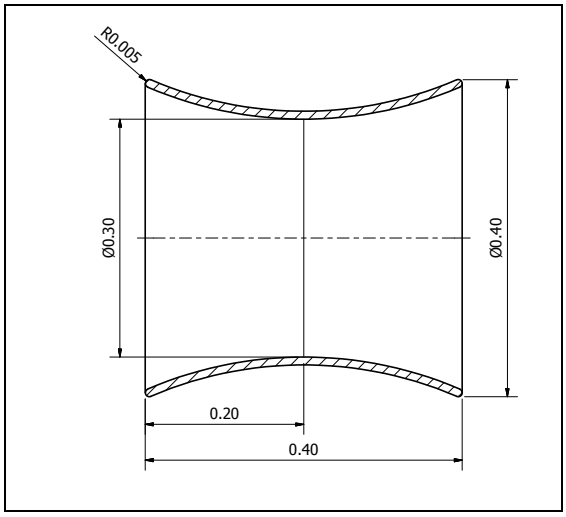

(C)

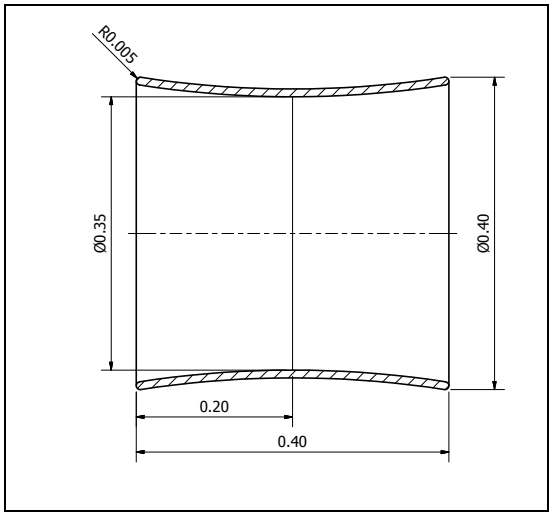

(D)

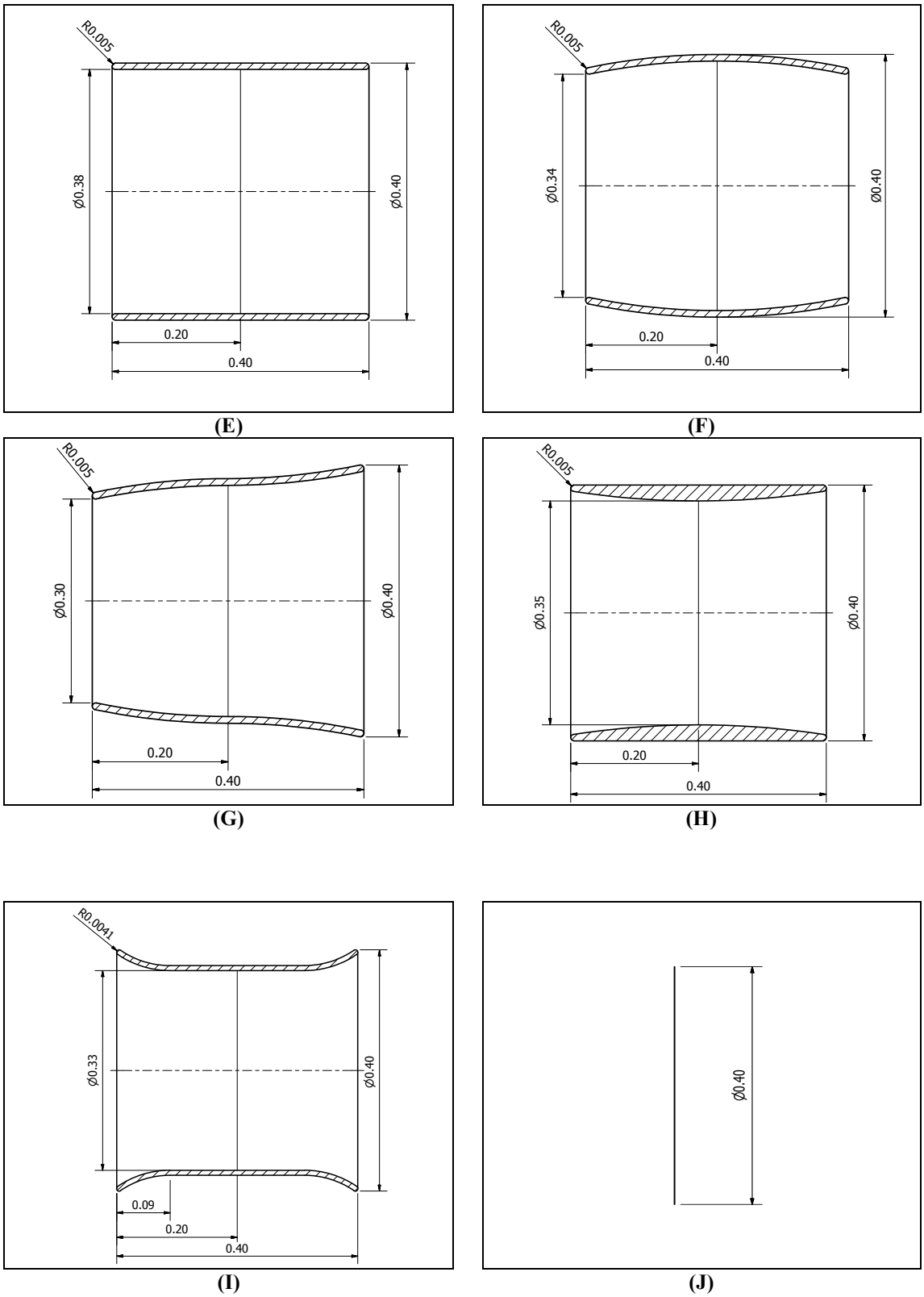

Figure 2.1.1: Schematic diagrams of (A-H) candidate duct designs, (I) Scaled approximation of a commercial design (AECOM 2009), and (J) Unducted device.

The effect of a hub* on rotor performance is also examined. An ellipsoidal geometry is chosen, with a major to minor axis ratio of 2:1. The volume of the hub is calculated via scaling arguments based on a commercial wind turbine (Vestas v100-3.0MW offshore), with the assumption that a linear relationship exists between hub volume and power.

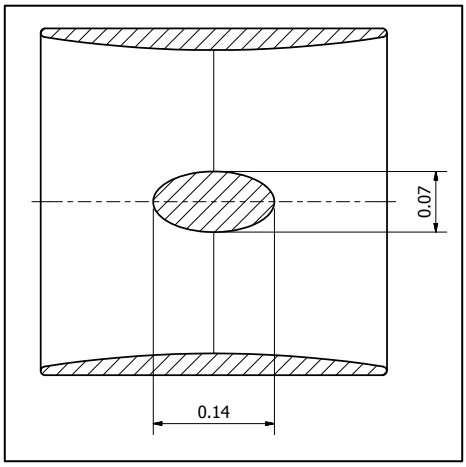

Figure 2.1.2: Ellipsoidal hub in position within duct H.

2.1.2 Performance Metrics

The coefficients of thrust and power are defined in Eqs. (2) and (3),

$$C_T = \frac{F}{\frac{1}{2}\rho A_{ref} u_\infty^2} \quad \textbf{(2)}$$

$$C_P = \frac{P_{disk}}{\frac{1}{2}\rho A_{ref} u_\infty^3} \quad \textbf{(3)}$$

where u_∞ is the freestream velocity and A_{ref} is the cross-sectional area based on the external diameter of the duct. We choose this dimension for reference to provide a constant comparative basis between candidate designs. We also

* In order to avoid confusion the outer shrouding is defined as a duct and the inner volume as the hub, as shown in Figure 2.1.2. The term nacelle is not used within this report.

believe that this is the fairest mechanism by which devices should be compared as it expresses power generated to that available in the streamtube intersected by the whole device; rotor together with its required external duct. Further, it is likely that depth will dictate external device dimension at many sites so that it is this dimension and not rotor diameter per se, that would be held constant in a candidate design study for a real tidal site.

Returning to Eqs. (2) and (3) the thrust F can be that of either the disk or duct, or the sum of both. The power extracted from the flow by the disk, P_{disk}, is calculated from Eq. (4)

$$P_{disk} = \int_{disk} \Delta p u_d \, dA \tag{4}$$

where u_d is the streamwise component of velocity at the disk. The pressure jump across the disk, Δp, is calculated by

$$\Delta p = K_L \frac{1}{2} \rho {u_d}^2 \tag{5}$$

where K_L is a dimensionless porous loss factor. Combining Eqs. (4) and (5) yields

$$P_{disk} = \frac{1}{2} K_L \rho \int_{disk} u_d^3 \, dA \tag{6}$$

The thrust exerted by the disk on the flow can be calculated in a similar manner.

$$F_{disk} = \frac{1}{2} K_L \rho \int_{disk} u_d^2 \, dA \tag{7}$$

The thrust exerted by the duct on the flow is retrieved directly from the flow solver, as are the integrated values in Eqs. (6) and (7).

The coefficient of power is a measure of disk power relative to the kinetic power available from the flow in the absence of the turbine. Power lost due to leading edge separation and wake mixing is not accounted for by the C_p metric. From a thermodynamic standpoint, the mixing of two or more streams of dissimilar velocities, as occur in turbine wakes between core and bypass flows,

will result in an increase in the mixed flow's entropy and hence represents a departure from the reversible state. Such losses are accounted for through the definition of a basin efficiency, defined here as the ratio of disk power to total power removed from the flow, as shown in Eq. (8). In order to conserve the finite tidal resource for other devices operating within the same tidal stream, a high basin efficiency is desirable.

$$\eta = \frac{\mathrm{P_{disk}}}{P_{disk} + P_{mixing}} \tag{8}$$

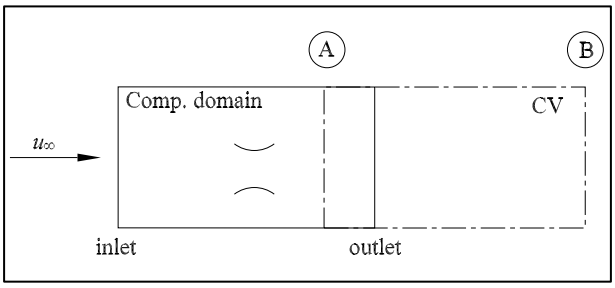

Figure 2.1.3: Control volume for calculation of basin efficiency.

The denominator in Eq. (8) is calculated by taking the difference between the energy fluxes through a plane upstream of the turbine and a theoretical plane far downstream (station *B*), where the turbine wake and bypass flows have fully remixed to establish a uniform flow velocity, thus representing the total power removal from the flow. Eq. (8) can thus be re-expressed as follows

$$\eta = \frac{\mathrm{P}_{disk}}{\int_{inlet} p_o \, u dA - \int_B p_o \, u dA} \tag{9}$$

where p_o is total pressure and u is the streamwise component of velocity. The total pressure p_o at station *B* can be calculated from conservation of horizontal linear momentum over a control volume downstream of the turbine spanning stations A to B (see Figure 2.1.3);

$$\int_A p \, dA - \int_B p \, dA = \int_B \rho u^2 dA - \int_A \rho u^2 dA \tag{10}$$

$$p_{o,B} = p_B + \frac{1}{2}\rho u_\infty^2 \tag{11}$$

where p is static pressure and conditions at station B are such that p_B is uniform and the flow velocity recovers to the upstream flow velocity, u_∞, recalling that we choose to use a fixed free surface height (rigid lid approximation). The inlet of the control volume, station A, is set between the turbine and the outlet of the computational domain as far upstream as is possible in order to minimize unphysical numerical dissipation losses. The analysis presented above is readily extendable to the case of a deforming free surface in which gravitational potential changes together with free surface height changes must be considered.

2.1.3 Solution Method

Simulations are carried out in a computational domain that is based on the flume at the EDF testing site. The dimensions of the model, laid out in Figure 2.1.3, are representative of a full-scale device operating within an array with an inter-device centre-to-centre spacing of $3.75D$ and a vertical blockage ratio of 40% resulting in an area blockage of b~8%.

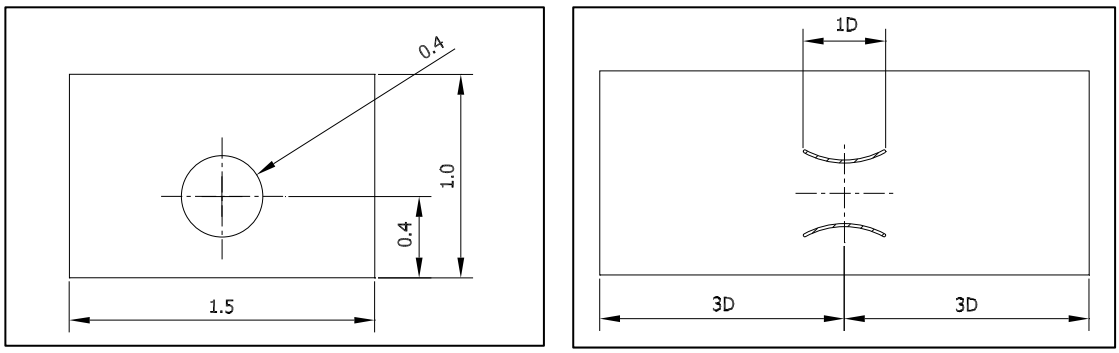

(a) **(b)**

Figure 2.1.4: Cross section of numerical domain, showing external duct diameter. (a) Section view through rotor plane, showing outer bounds of device. (b) Side view, with flow moving from left to right.

The inlet boundary is set three diameters upstream of the rotor plane. Flow uniformity upstream of the turbine, mass conservation due to the bound nature of tidal flows, and low inflow grid density permit this heuristic choice of boundary placement. The influence of the downstream boundary on wake development and hence turbine performance is an area where appreciable

savings in computational cost can be made without sacrificing solution accuracy.

In WP3 WG1 D1 outflow placement of six diameters was found to be satisfactory in terms of solution accuracy. However to improve solution time, a requirement of such a broad parametric study, reductions in overall cell count are sought. To determine the effect of outlet distance, four computational domains are investigated, with distances of three, six, twelve and twenty-four diameters downstream of the rotor plane. These simulations are carried out on device D at operating points associated with peak thrust and peak power. For all boundary distances trialled, static pressure is found to be invariant at common planes 1D, 2D and 3D downstream of the rotor. Accordingly, a vanishingly small change in rotor performance due to downstream placement is observed, as shown in Figures Figure 2.1.5 and Figure 2.1.6.

Note that in order to make cross-comparisons between different domain lengths the upstream pressure must be constant. Hence, in all cases the static pressure field has been corrected to achieve zero static pressure at the domain inlet. This results in negative static pressures aft of the turbine and total pressure, p_o, being less than dynamic, p_{dyn} , as $p_o = p + p_{dyn}$.

In Table 2.1.1, the power and thrust coefficients for device D operating at peak power are compared, for the same series of computational domain lengths. The percentage differences are presented relative to the results computed for the longest downstream domain length, and in each case is less than 0.25%.

A downstream domain length of three diameters is deemed to be satisfactory, based on the results of these comparisons, and is used for all subsequent simulations.

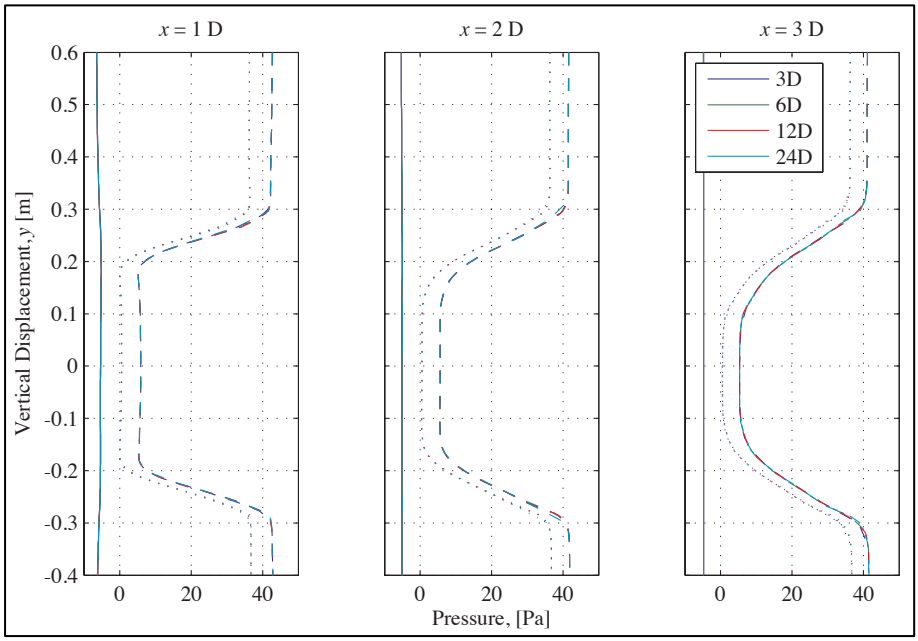

Figure 2.1.5: Cross-stream profiles of static pressure (solid lines), dynamic pressure (dashed lines) and total pressure (dotted lines), for downstream domain lengths of 3, 6, 12 and 24 D. Results are for device D operating at peak thrust. Static pressure is 0 at inlet.

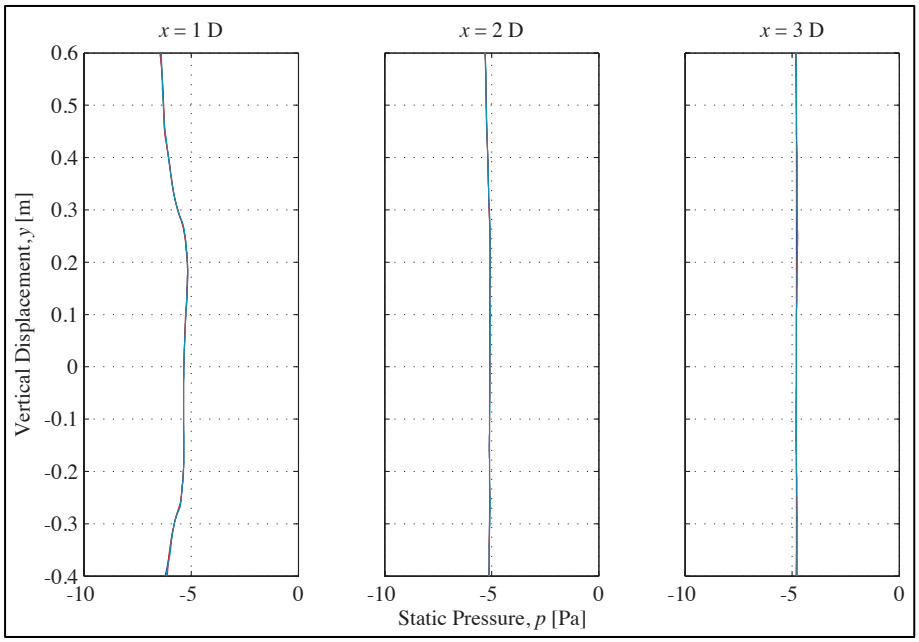

Figure 2.1.6: Close up of cross-stream profiles of static pressure for downstream domain lengths of 3, 6, 12 and 24 D. Results are for device D operating at peak thrust. Static pressure is 0 at inlet. Line colours correspond to the legend in Figure 2.1.5.

x/D	C_P	Difference	C_T	Difference
24	0.420758	0.00%	0.512683	0.00%
12	0.421261	0.12%	0.513135	0.09%
6	0.420772	0.00%	0.512741	0.01%
3	0.419744	0.24%	0.511690	0.19%

Table 2.1.1: Comparison of power and thrust coefficients for simulations of device D operating at peak power, with downstream domain lengths of 3, 6, 12 and 24 D.

A velocity of 0.27 $m\ s^{-1}$ is set at the inlet, corresponding to velocity condition *U0* for the flume experiments. A gauge pressure of 0 *Pa* is set across the outlet. The floor and sidewalls are modelled as slip walls replicating the zero penetration / symmetry conditions present in the EDF flume. The free surface is modelled as a rigid lid. The use of a rigid lid in place of a free-surface condition is considered sufficient for the low blockage conditions of $b \sim 8\%$ under study (Consul et al, 2011).

The focus of this series of simulations is on capturing the hydrodynamics of the duct effectively. Local flow features pertaining to the rotor, such as swirl and blade loading, are of lesser significance at this stage. The axial thrust of the rotor is important and must be modelled. Computational load is also a primary concern, as many candidate duct geometries must be simulated for a full range of operating points. These requirements can be met by modelling the rotor as a porous disk.

A pressure jump is applied across the disk, with a stream-wise loading dependent on local velocity and a porous loss factor K_L as defined previously in Eq. (5). The full range of disk operating points is achieved by varying K_L from 0 to 4.

2.1.4 Mesh Generation

The mesh is generated using a highly automated method, where basic cell dimensions are specified at boundaries, surfaces and density regions, and the domain is filled according to the octree algorithm (Ansys, 2010). The resulting unstructured mesh is unique, and cannot be reproduced exactly if the geometry is modified. Some degree of control over the mesh topology is relinquished in favour of robust and efficient mesh generation. While coordinates of cell nodes and centroids will not individually correspond between meshes, general regions of specified resolution will. In any given comparison between solutions for different duct geometries, there will be slight differences in node placement. However, overall grid topology remains consistent, as illustrated in Figure 2.1.7.

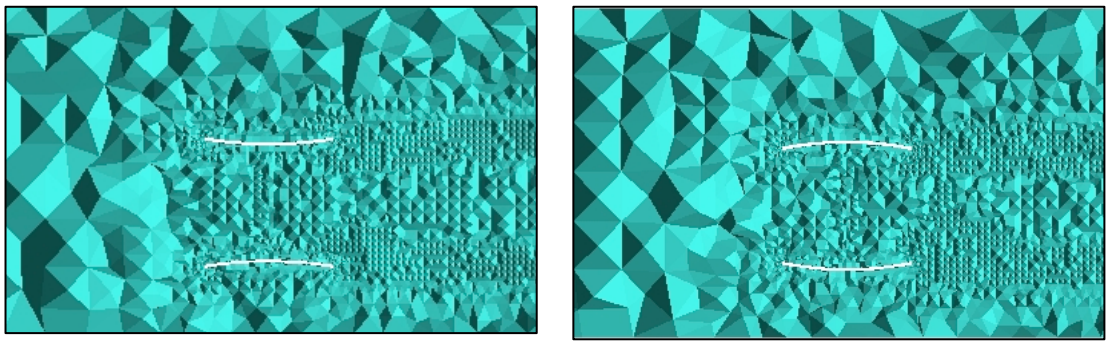

(a) **(b)**

Figure 2.1.7: Corresponding cell density regions are visible in the wake for (a) duct D, and (b) duct F are visible in these close-up views.

2.1.5 Spatial Resolution

Mesh resolution is highest where regions of highest velocity gradient are expected. In order to fully resolve the boundary layer on the duct surface, the wall-adjacent cell height is set to achieve a y^+ value of 1.0. This non-dimensional wall distance is defined as

$$y^+ = \frac{y}{\nu}\sqrt{\frac{\tau_w}{\rho}} \qquad (12)$$

where τ_w is the wall shear stress, y is normal distance from the wall, and ν is

kinematic viscosity. Upon examination of the solution flow fields, regions of over- and under-resolution are identified. Under-resolved regions include the free-shear layers adjacent to the duct exterior and downstream of the trailing edge. The low-velocity core of the wake is over-resolved. For subsequent simulations, carried out on ducts D, E, F, and H, mesh density in these regions is modified appropriately. The qualitative result of these alterations to mesh topology is illustrated in Figure 2.1.8, where resolution of the leading edge shear layer has been improved. However, little quantitative difference is observed in the force coefficients. This improved mesh is used as the base case for the mesh refinement study, which is carried out on device D operating at maximum thrust.

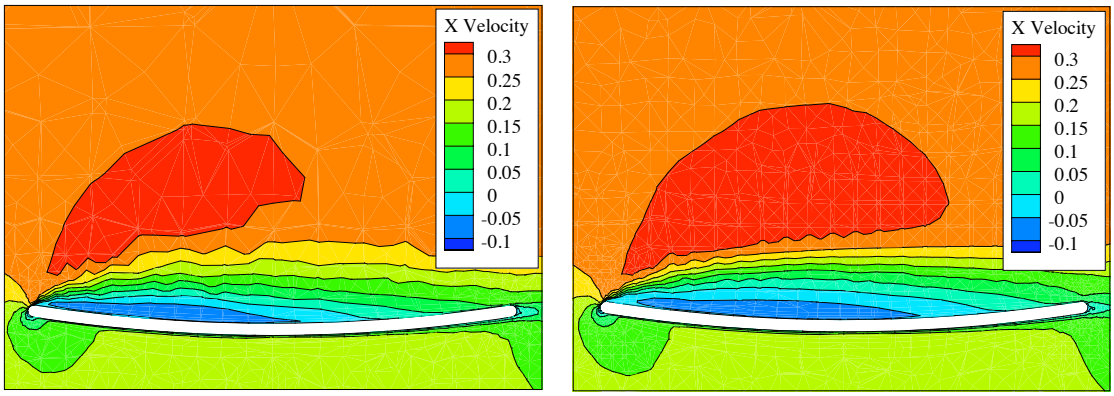

(a) **(b)**

Figure 2.1.8: Mesh refinement to resolve leading edge shear layer. Contours are coloured by streamwise velocity in metres per second. Flow direction is from left to right.

As the mesh is generated using an automated method (cf. Section 2.1.4), spatial refinement is carried out by applying a global scaling factor. The cell size specifications throughout the domain are multiplied by this factor, and a new mesh is produced with the resolution scaled accordingly. An increase in scaling factor results in an increase in local cell size, and decrease in mesh density.

Integrated performance metrics, such as the coefficients of thrust and power, are found to be insensitive to mesh resolution for all cases trialed. A more informative comparison can be made based on distributed variables, where local effects of mesh resolution are highlighted.

In Figure 2.1.9, the influence of mesh resolution on the pressure distribution about duct D is evident. A prominent feature of this figure is the pressure jump

across the disk. This pressure jump must be applied across the centroids of the cells directly upstream and downstream of the disk. The distance between cell centroids is smallest for the high-resolution mesh, leading to a steeper gradient in pressure across the disk. The magnitude of the pressure jump however is not affected. Mesh resolution effects are evident in the reattachment region on the suction (external) surface of the duct. The difference between the medium and low-resolution meshes is greater than that between the medium and high resolution meshes (see rear section of suction surface).

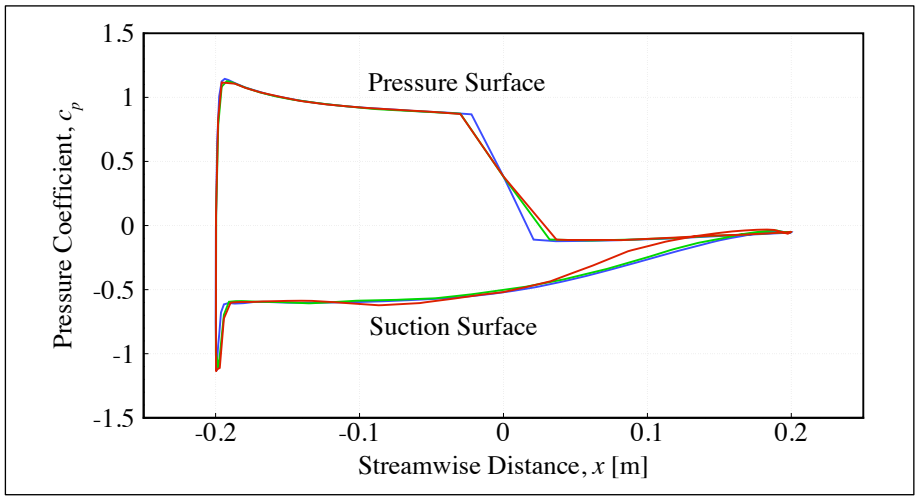

Figure 2.1.9: Distribution of pressure coefficient around a cross-section of duct D, operating at an induction factor a = 0.5, with three levels of mesh resolution. Duct cross-section is taken horizontally at the centreline, in the positive-z direction. — Low resolution; — Medium resolution; — High resolution.

The relative differences between meshes are also highlighted in Figure 2.1.10, in which a series of wake static pressure profiles are laid out. These profiles are taken along vertical traces through the midplane of the domain, at locations *0.5D*, *1D*, *2D* and *3D* downstream of the disk. The first location coincides with the duct trailing edge, and the final location is at the outlet of the domain.

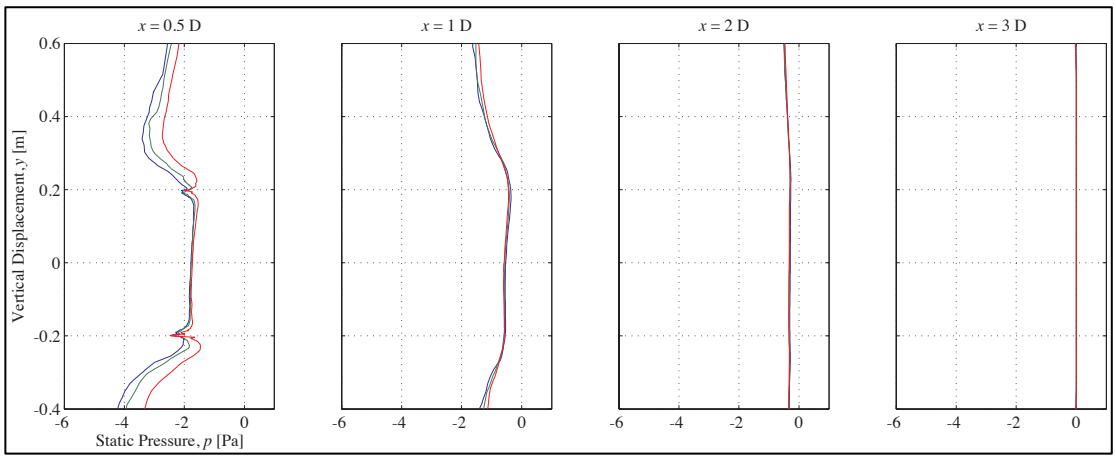

Figure 2.1.10: Vertical centreline profiles of static pressure at four locations downstream of device D, operating at induction factor of 0.5. — low resolution; — medium resolution; — high resolution.

The conclusion drawn from the results in Figure 2.1.9 and Figure 2.1.10 is that the mesh resolution can be reduced generally by a global scaling factor of 1.5 (medium resolution case), with only a small effect on the pressure field. This scaling factor is applied uniformly to the base mesh, but resolution is maintained at the leading and trailing edges of the duct to capture those small scale geometric features.

2.1.6 Temporal Resolution

Steady simulations are generally less computationally expensive than unsteady simulations, and hence are favoured in cases where solutions are time-invariant (steady), or where the average of a time-dependent (unsteady) solution captures all significant flow-features. To determine whether the series of duct designs in question can be modelled in the steady (time averaged) state, a comparison is made between steady and unsteady calculations of device performance. Device D, operating at high thrust, is chosen as a test case. The performance parameters of interest are the coefficients of thrust and power.

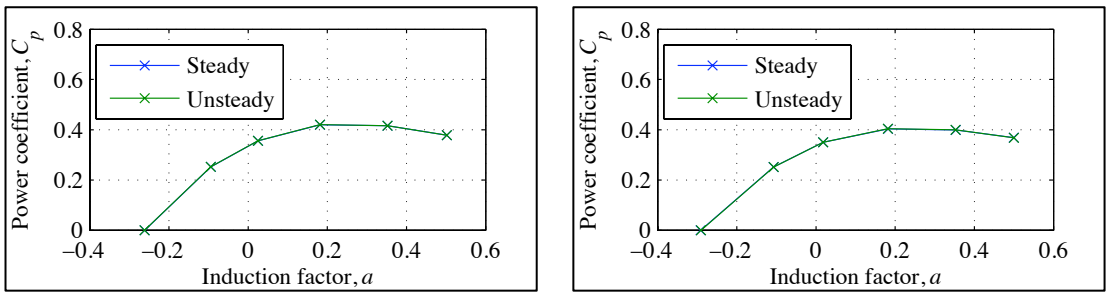

(a) **(b)**

Figure 2.1.11: Comparison of power coefficient of device D for steady and unsteady simulations (a) without hub, and (b) with hub.

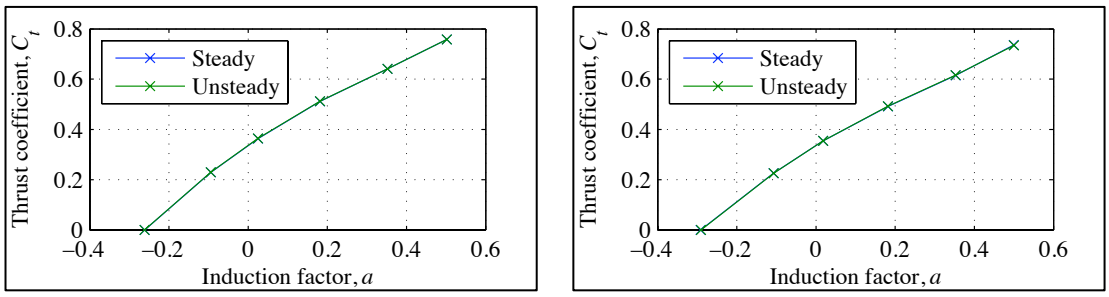

(a) **(b)**

Figure 2.1.12: Comparison of thrust coefficient of device D for steady and unsteady simulations (a) without hub, and (b) with hub.

While unsteady flow features exist downstream of the duct and hub, which cannot be resolved locally by steady simulation, the effects on the coefficients of thrust and power are negligible. The conclusion here is that unsteadiness in the wake does not discernibly influence the flow at the rotor plane. Calculation of device performance can therefore be made with confidence by steady simulation.

2.2 Results

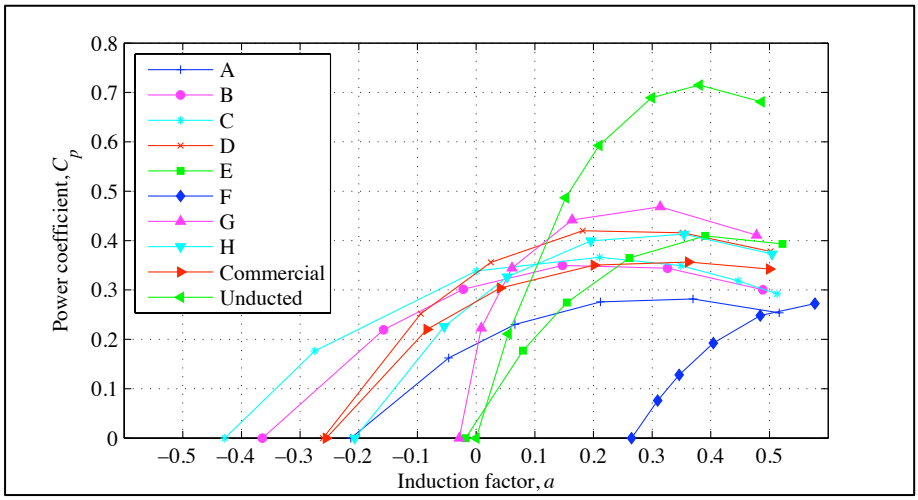

Figure 2.2.1: Power coefficient plotted as a function of induction factor for the series of preliminary duct designs. Note the performance of the unducted porous disk, which is included for reference.

Figure 2.2.1 shows the how ducts A – H, a scaled commercial design, and an unducted rotor perform relative to each other. The results for ducts D and H have been calculated using refined meshes (cf. Section 2.1.5). The most prominent curve is that of the unducted rotor, which outperforms the best bi-directional design, device H, by about 75%. Of the ducted devices, the unidirectional device G performs best. The duct is required to be bidirectional, and of those designs ducts D, E and H show most promise. Note that the Betz limit of $C_p \approx 0.593$ is applicable only to unbounded flow.

One effect of a converging-diverging duct (A, B, C, D, G, and H in Figure 2.2.1) upon a rotor is to broaden the operating range into the negative induction factor region, indicating an acceleration of disk flow velocities to magnitudes greater than freestream. The curved surface of the duct accelerates the internal flow beyond the freestream velocity. While an increase in curvature leads to a desirable increase in disk velocity, it also necessitates an undesirable reduction in disk diameter. An optimum duct curvature exists which achieves the best balance between flow acceleration and power-extracting area. Of the ducts investigated in this comparison, the internal curvature of ducts D and H (same) is

found to be the best performing of those tested.

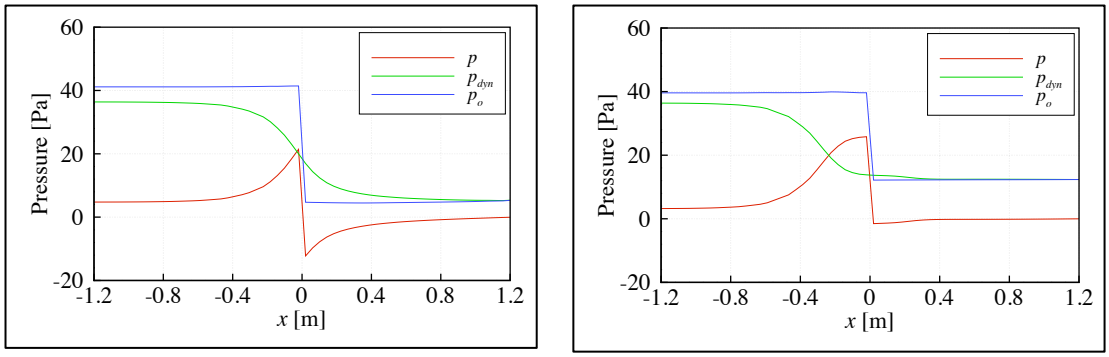

(a) **(b)**

Figure 2.2.2: Pressure profiles along the centreline for (a) the unducted case and (b) device E. In figure (b), the static pressure does not fall far below zero downstream of the disk.

Despite the fact that the disk of device E is nearly the same size as the unducted case, it yields a lower power coefficient. Examining the centreline pressure profiles for both devices, shown in Figure 2.2.2, it is clear that the duct limits the drop in static pressure across the disk. Velocity stream-traces are superimposed on the pressure field through the vertical midplane of each device in Figure 2.2.3 (a) and (b). For the ducted device, trailing edge flow separation, indicated by the parallel streamlines for both internal and external flows, prevents local flow curvature. Hence the pressure gradients observed downstream of the unducted device cannot be supported downstream of the ducted device, resulting in the limited pressure drop illustrated in Figure 2.2.2 (b).

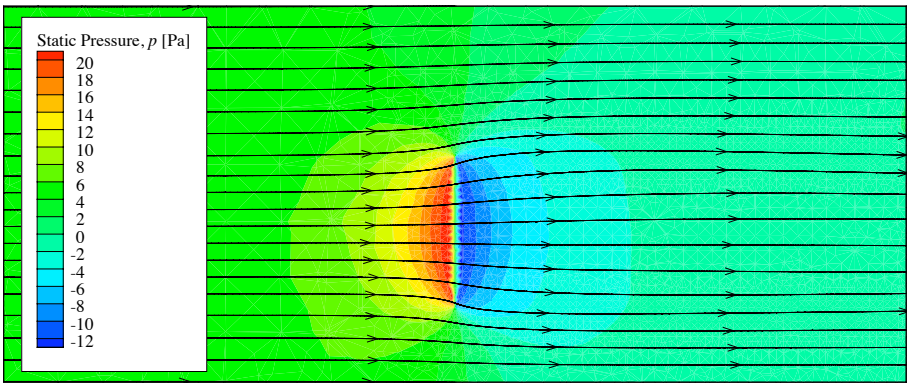

(a)

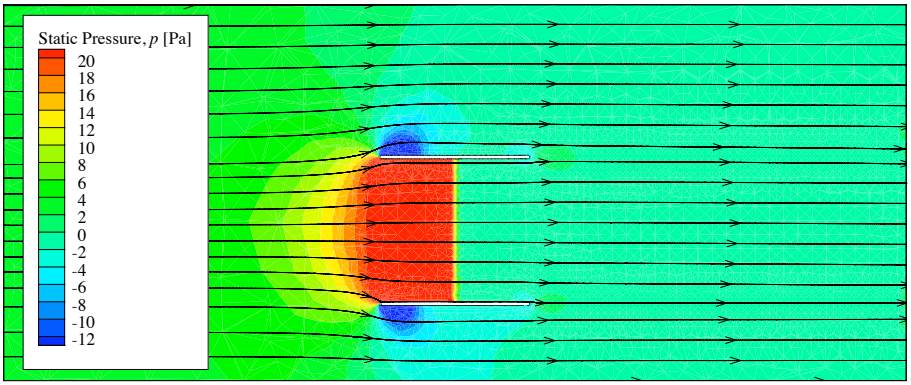

(b)

Figure 2.2.3: Contour plots of static pressure at the vertical midplane of (a) the unducted case and (b) device E. The streamtraces in (b) show that the flow is prevented from expanding downstream of the disk.

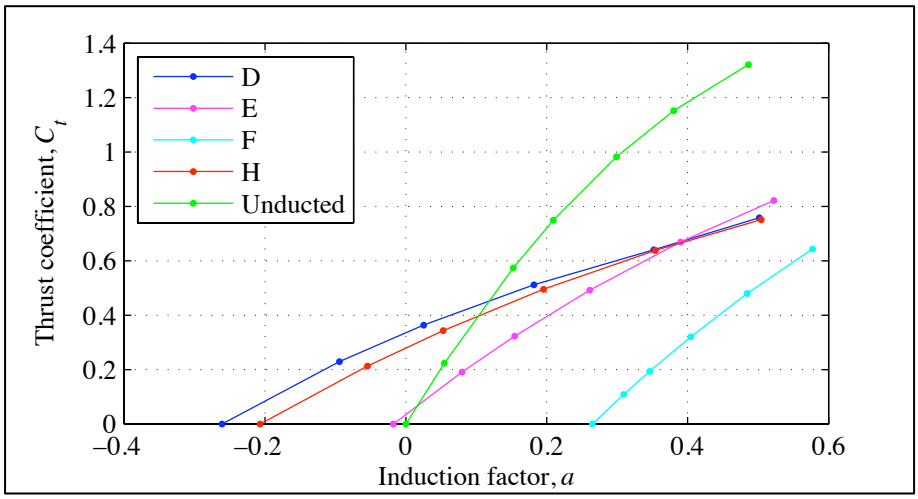

(a)

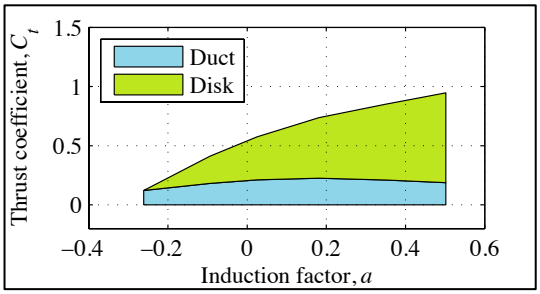

(b)

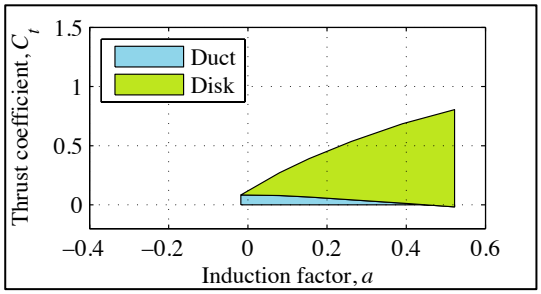

(c)

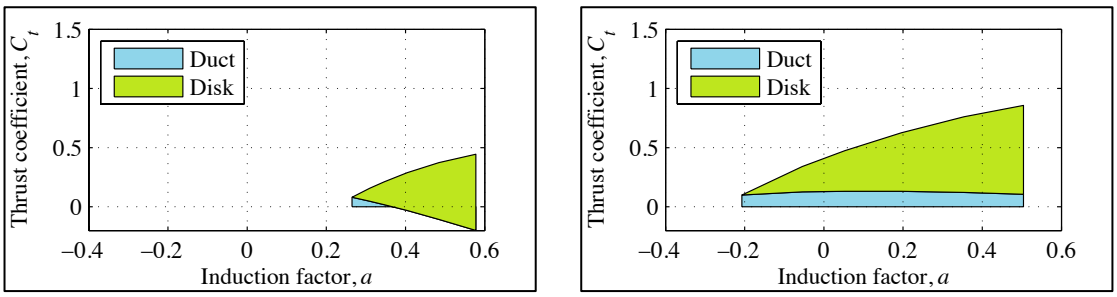

Figure 2.2.4: Comparison of thrust coefficients for devices D, E, F, and H, showing (a) disk thrust only, as well as cumulative components of thrust for (b) device D, (c) device E, (d) device F, and (e) device H.

Device thrust is compared in Figure 2.2.4, with the contributions from the disk and duct shown individually. Power extraction is associated with disk thrust. High duct thrust results in flow separation at the leading edge of the duct, which increases effective blockage (Belloni & Willden, 2010). Ducts E and F exhibit low duct thrust at maximum disk loading, which may be desirable at the basin scale. In devices E and H, the flat external surface reduces the size of the separated region, decreasing momentum loss in the flow. This in turn acts to reduce the thickness of the re-attached boundary layer external to the duct surface, thus leading to reductions in form drag. These reductions are illustrated in Figure 2.2.4 with ducts E and H (flat exterior) both reporting lower thrust coefficients than duct D (concave exterior). Leading edge separation is delayed by the negative camber of duct F.

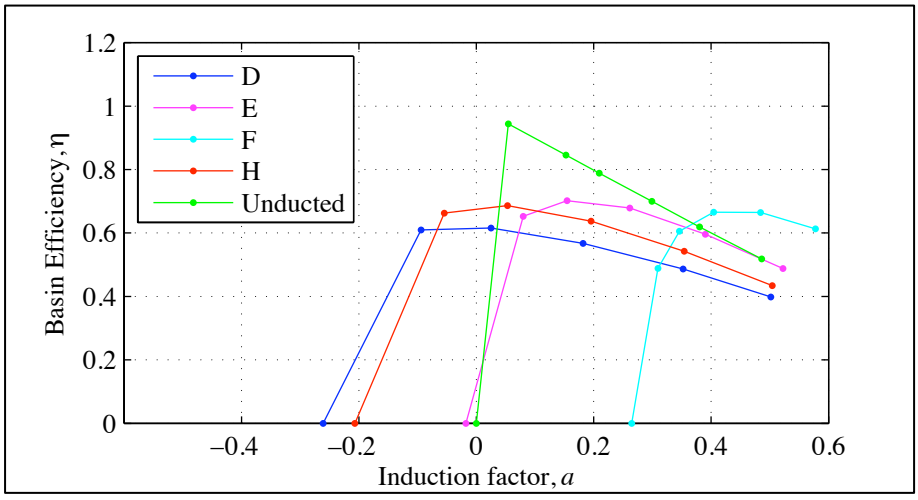

Figure 2.2.5: Comparison of basin efficiency for devices D, E, F, and H.

Figure 2.2.5 shows that the unducted device performs best in terms of basin efficiency. The other devices generally have lower basin efficiencies due to the additional loss mechanisms associated with added streamwise loading, or drag, on the duct. There is little difference between the peak efficiencies of devices E, F and H, while device D performs least well.

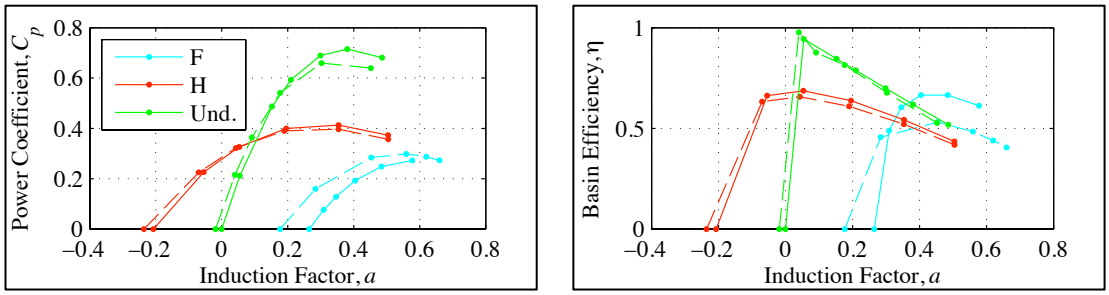

Figure 2.2.6: Effect of hub on (a) power coefficient, and (b) basin efficiency. — without hub; - - - with hub.

Figure 2.2.6 shows the effect of a hub on device performance. The additional blockage generated by the hub leads to an increase in local velocity at the disk for a given thrust. Peak power is reduced in correspondence to the reduction in disk area.

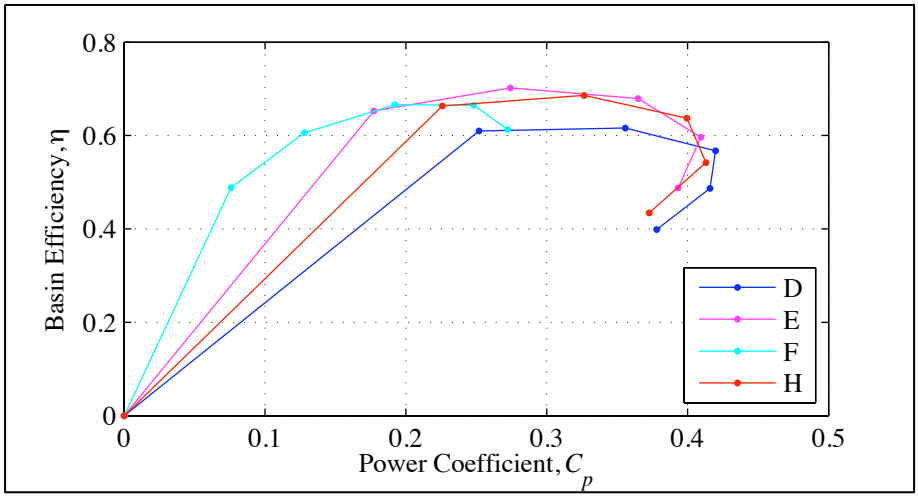

Figure 2.2.7: Comparison of basin efficiency and power coefficient for a selection of ducted devices.

A tidal turbine can be optimised by maximising power coefficient and basin efficiency. These two parameters are plotted in Figure 2.2.7 for a range of

devices. For each device, the operating point closest to the top right-hand corner of the graph is optimal. In the case of device H, a significant increase in basin efficiency may be achieved at the expense of a small reduction in power. By example, when the disk loading is reduced by 22.4%, the basin efficiency increases by 16.3%, while the power produced only drops by 3.2%, as shown in Table 2.2.1.

	Operating Point 1	**Operating Point 2**	**Difference**
C_t	0.6383	0.4953	-22.4%
C_p	0.4129	0.3995	-3.2%
η	0.5423	0.6307	+16.3%

Table 2.2.1: A 16.3% gain in efficiency may be achieved by operating device H slightly off its peak power operating point.

2.3 Conclusion

The aim of this body of work has been to design the duct for a ducted tidal turbine. Of the range of ducts studied, duct H is selected, as it achieves the best balance of power coefficient and basin efficiency for a tidal device.

Subsequent to the commencement of this study into ducted device design, a rotor diameter of 27 cm was chosen by the consortium. As the rotor diameter of device H is 35 cm, a scaling factor of $\frac{27}{35}$ is applied, resulting in the duct geometry shown in Figure 2.3.1.

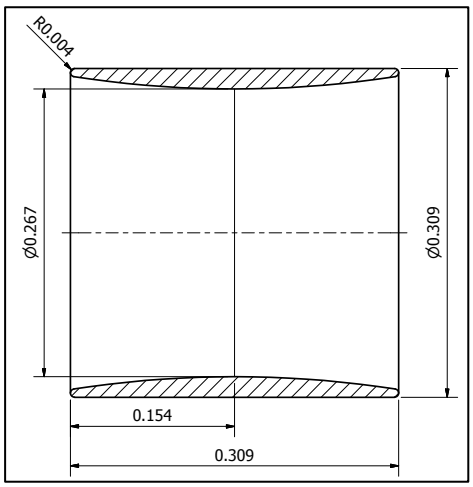

Figure 2.3.1: Duct H scaled to fit a 27 cm diameter rotor.

3 Rotor Design

Within work package WG1 WP3, a 60 cm diameter rotor is being simulated, with complementary experiments being carried out in WG4 WP1. It is not feasible to append a duct to this rotor for testing in the EDF flume, as the blockage ratio would be unrepresentative of full-scale installation conditions. Elsewhere within the PerAWaT project, a 27 cm diameter rotor has been tested (WG4 WP2 D2). The design of a ducted device utilising this rotor will result in a more reasonable blockage ratio when operating in the EDF flume and is hence considered a suitable candidate for use within the current work package.

Rotor ducting and flow blockage is known to significantly alter the local flow environment at the disk (Figure 2.2.3). Ducting prevents local flow deceleration, bounding the flow field and limiting streamline curvature towards the rotor tips. In addition, tip losses associated with helical vortex structures generated by unducted rotors, are avoided. The absence of discrete tip vortex structures for ducted devices is discussed in Section 4.4.

It is expected that a rotor designed specifically for the altered flow environment within a duct would out-perform a rotor that has been specifically designed for unducted operation. As such, and to complement the design of a duct presented in Section 2.2, the bespoke design of a rotor (distribution of twist and taper) specifically tailored for operation within a blocked / ducted environment is undertaken, the results of which are presented below.

3.1 Blade Element Momentum Method

Widespread and continued use of one-dimensional analytical blade element momentum methods (henceforth referred to as "analytical BEM") across both academic and industrial sectors is testament to the value of the technique as an accurate and computationally efficient wind turbine performance prediction tool. Whilst most suited to cases presenting an unbounded uniform inflow, modifications to the baseline analytical method have been made (Hansen 2008) to incorporate a number of secondary flow features such as: moderate vertical velocity shear; tower shadow and unsteady inflows. Unfortunately, as the

perturbation size away from a uniform unbounded inflow is increased, assumptions implicit within the model are seen to breakdown and other methods, capable of accurately modeling large departures from the uniform flow condition, are sought.

In blade element momentum (BEM) theory, the rotor is modelled as a series of concentric annuli, operating in unbounded flow. At each radial station, the axial and swirl induction factors and the angle of attack are calculated. Look-up tables are used to find the corresponding coefficients of lift and drag, provided by wind tunnel experiment, from which the resultant blade forces are resolved. The procedure is repeated iteratively until the angle of attack, induction factors and blade forces settle and a converged solution results.

3.1.1 BEM Embedded within CFD Solver

The blade element momentum method is implemented as a boundary condition within a FLUENT simulation, in an analogous manner to the porous disk model detailed in Section 2.1.3. The axial and tangential forces imparted by the rotor on the flow can be reproduced, without the computational cost associated with the explicit modelling of the rotor geometry. As BEM does not account for discrete blades, the forces at each radial station are averaged circumferentially. In certain cases, this leads to a steady flow field, which can be calculated using the steady form of the RANS equations. Hence, further reduction in computational cost can be achieved.

3.1.2 Validation

In order to verify the embedded BEM method against analytical BEM, an effectively unbounded rotor (1% blockage) is simulated. To replicate the analytical BEM solution, where no flow is modelled inboard of the first radial annulus, the computational model is constructed to include a cylindrical slip wall boundary inside the first radial station. This cylindrical inner boundary extends from the inlet to the outlet of the domain directly replicating the solution achieved using the analytical method.

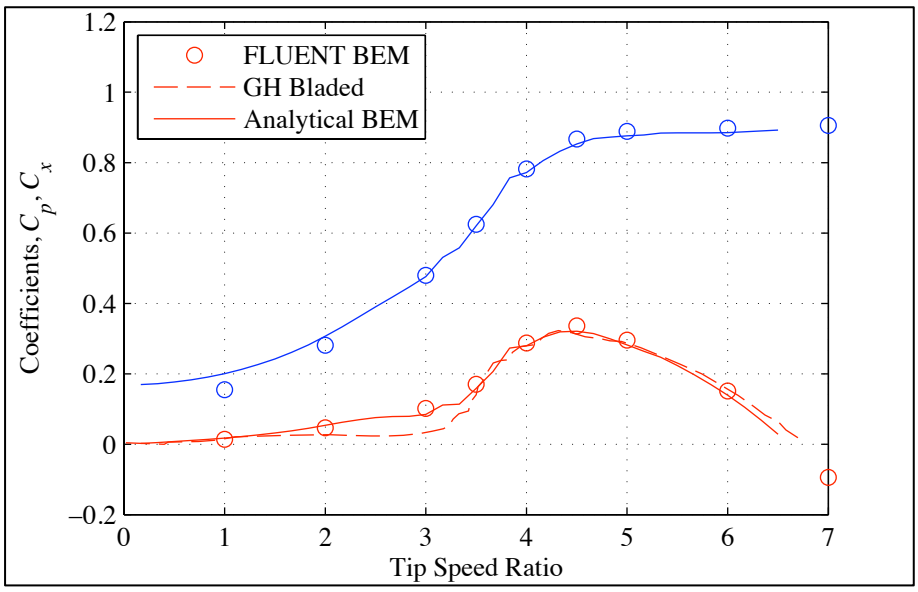

Figure 3.1.1: Comparison of BEM embedded in FLUENT, Garrad Hassan BLADED, and analytical solution. — Power coefficient; — Thrust coefficient.

Details of the validation methods are given in Section 3.2. Figure 3.1.1 illustrates a good agreement between BEM embedded within a steady FLUENT simulation (RANS-BEM) and the analytical solution. At low tip-speed-ratios, disagreement is visible between the analytical (Oxford) / RANS-BEM and GH Bladed results. Operation at low tip-speed-ratios (defined as being lower than that coincident with maximum Cp) results in large blade local angles of attack, frequently exceeding stall. For the case of deep stall, aerofoil performance is invariant over a wide range of practical sectional profiles and Reynolds numbers. This fact, combined with a frequent lack of 2D experimental blade data in the post-stall region. permits the use of analytical models of post-stall aerofoil performance. The Oxford BEM methods employ the widely accepted post-stall model by Viterna and Corrigan (1981). Significant differences between the Oxford and GH analytical BEM generated power curves are only apparent at low tip-speed-ratios and are likely due to choice of post-stall model. The verification of the embedded RANS-BEM model is not affected.

A potential advantage of RANS-BEM is that rotor performance could be predicted with a steady simulation, thus greatly reducing computational effort. Uncertainties arise in the steady simulation where unsteady features such as

temporal vortex formations in the wake are not resolved. To investigate whether the neglect of such features impacts negatively on the prediction of rotor performance, a comparison of steady and unsteady simulations are carried across a spread of three tip-speed-ratios, as shown in Figure 3.1.2 and further reproduced in Table 3.1.1 detailing relative percentage errors between each solution method.

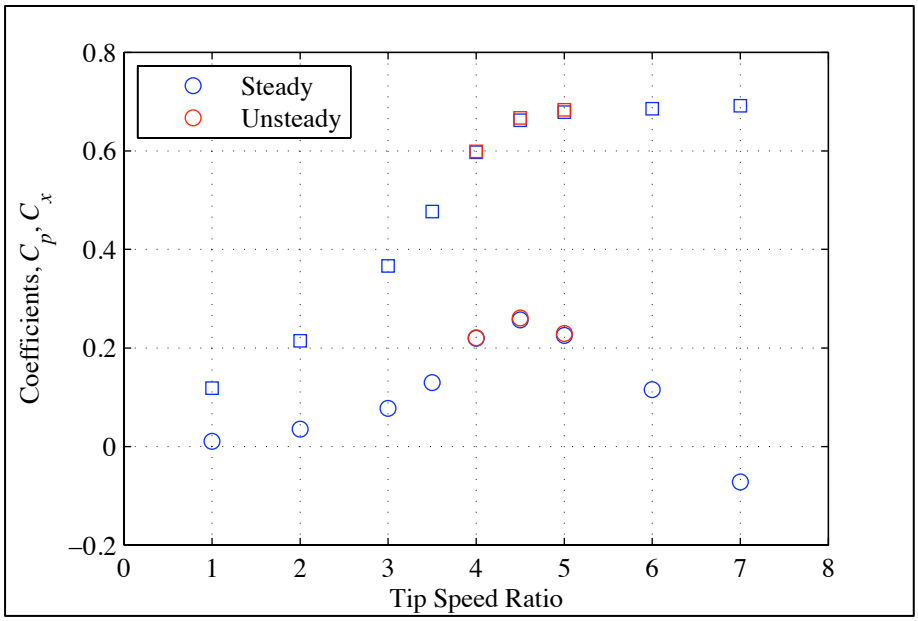

Figure 3.1.2: Comparison of steady and unsteady simulations for FLUENT-embedded BEM.

TSR	Metric	Unsteady	Steady	Relative Error
4.0	C_p	0.2884	0.2878	-0.21 %
	C_x	0.7834	0.7820	-0.18%
4.5	C_p	0.3416	0.3363	-1.55%
	C_x	0.8734	0.8671	-0.72%
5.0	C_p	0.3004	0.2952	-1.73%
	C_x	0.8950	0.8890	-0.67%

Table 3.1.1: Comparison of steady and unsteady simulations for FLUENT-embedded BEM.

3.2 Ducted Rotor Design

Introduced and validated in Section 3.1**,** the technique of embedding the BEM method, incorporating pre-determined aerofoil lift and drag data, within a RANS solver is shown to perform very well when compared to trusted industry standard analytical techniques (Figure 3.1.1). A significant advantage of the RANS-BEM method is its ability to correctly account for major flow field interactions such as: extreme flow blockage and free surface proximity including the effects of free-surface waves; turbine – turbine interactions; significant vertical velocity shear; and ducted device operation.

Within the following section, the developed RANS-BEM technique is applied to the bespoke design of a ducted rotor operating within the EDF water flume facility. The influence of both flow blockage and rotor ducting on rotor performance is first presented, with comparisons made to an analytical unbounded BEM solution employing the University of Manchester (UoM) 1/70th scale rotor. A strategy for rotor design based on equally distributed stream-wise load is then presented. This method is first tested for an un-ducted rotor operating within the flume, with the effectiveness of the developed design tool rated against the performance of the base-line (UoM) rotor. A rotor design is

then pursued for a ducted case utilizing the duct H geometry (Figure 2.3.1). Comparisons between the ducted and un-ducted geometrical rotor designs are then made. Finally, the rotor designed for unducted operation is placed within duct H to quantify the importance of including the influence of ducting in the evolution of a ducted rotor design.

3.2.1 Departures From Unbounded Flow

A comparison between the unbounded analytical BEM and RANS-BEM methods is now made to better illustrate the influence of blockage and ducting on rotor performance. As the analytical BEM method used is not capable of incorporating the effects of blockage and ducting the unbounded result is presented for the analytical BEM case.

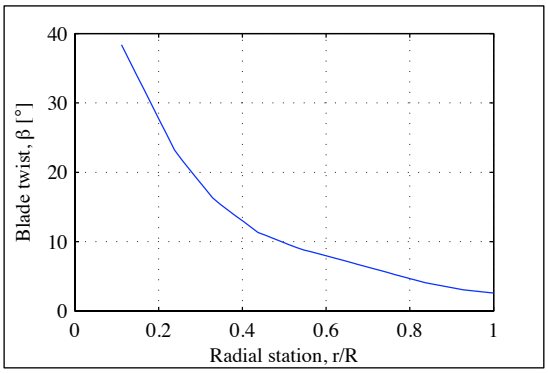

Figure 3.2.1: Illustration of blade twist distribution for baseline UoM geometry.

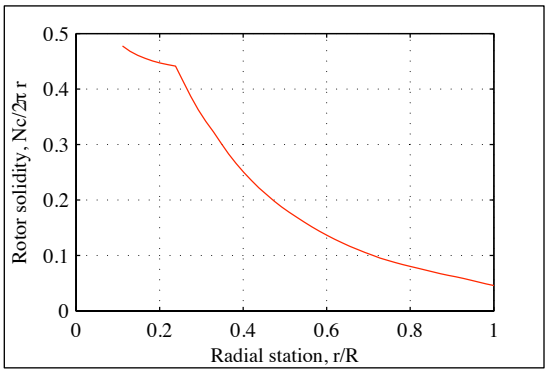

Figure 3.2.2: Illustration of local solidity distribution for baseline UoM geometry.

The baseline UoM rotor geometry is used as a starting point for the ducted rotor design. This geometry is presented in Figure 3.2.1 and Figure 3.2.2, illustrating blade twist and local solidity respectively. Further details of the UoM rotor design can be found in WG4 WP2 D2 and WG4 WP2 D3. Aerofoil data for the Goettingen 804 aerofoil operating at a Reyolds number of 30,000 is provided by the Hassan (1993) data set and is reproduced here in Figure 3.2.3 and Figure 3.2.4. Geometrical details of the EDF flume are given in Figure 2.1.4 along with a full description of the duct H geometry in Figure 2.1.1. Both the analytical BEM and RANS-BEM methods have been validated against the GL Garrad Hassan wind turbine performance prediction method, GH Bladed (Bossanyi, 2003), presented

in WG3 WP1 D1 and Section 3.1.2 respectively.

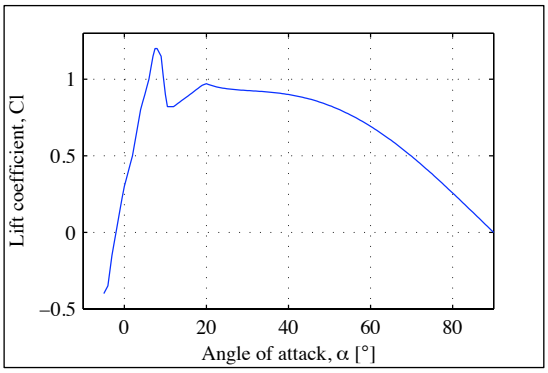

Figure 3.2.3: Illustration of experimental Goe804 aerofoil lift data along with the Viterna-Corrigan post stall model (Hassan 1993, Re 30,000).

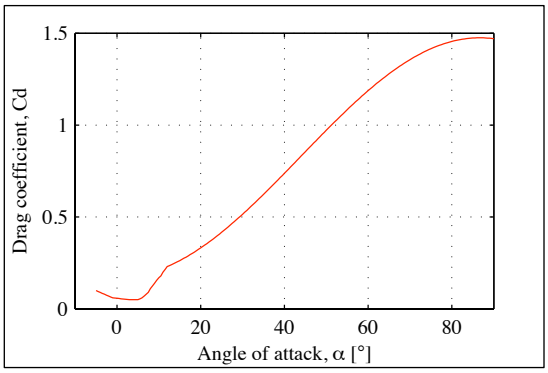

Figure 3.2.4: Illustration of experimental drag data for the Goe804 aerofoil along with the Viterna-Corrigan post stall model (Hassan 1993, Re 30,000).

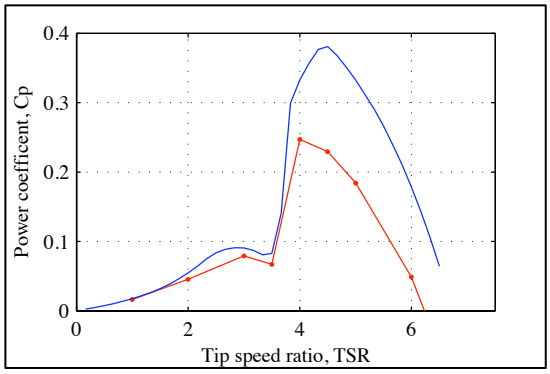

Figure 3.2.5: Illustration of the effects of blockage and ducting on rotor power.

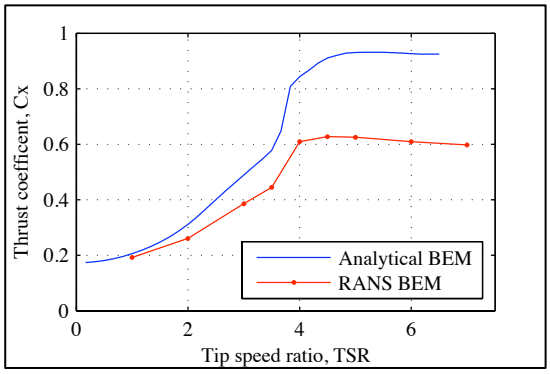

Figure 3.2.6: Illustration of the effects of blockage and ducting on rotor thrust.

Figure 3.2.5 and Figure 3.2.6 illustrates a comparison between analytical and RANS-BEM methods applied to a blocked ducted rotor flow*. Rather than an isolated study into either the effects of blockage or ducting, the results presented here aim to portray significant differences arising in the prediction of rotor performance using each technique; hence justifying the requirement for a design

* To aid comparison between the analytic and RANS-BEM methods, both solutions undertaken here are solved without the use of a tip-loss model. Typically unducted simulations would employ such a model whilst ducted solutions would not (verified in Section 4.4).

method capable of encapsulating significant additional flow features that occur within tidal flows. The rotor power and thrust curves, shown in Figure 3.2.5 and Figure 3.2.6 illustrate distinctly different performance predictions both in terms of overall shape and value. Application of blockage and ducting leads to a decrease in maximum predicted power of ~23% along with a slight widening of the power curve and the movement of the maximum power point to a lower tip speed ratio. This reduction in predicted power output is accompanied by a corresponding reduction in thrust coefficient. The difference between performance predictions by RANS-BEM and analytical BEM is a function of tip speed ratio and has a maximum magnitude of ~33%.

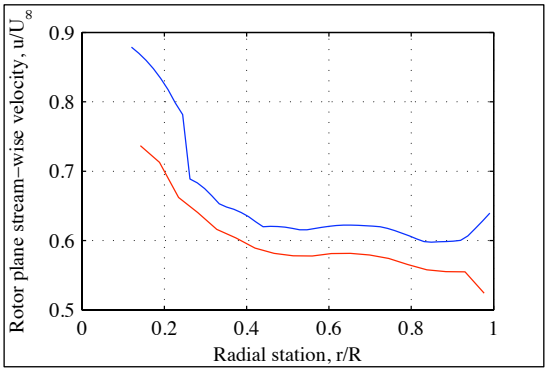

Figure 3.2.7: Illustration of the effects of blockage and ducting on rotor axial velocity at the rotor plane (λ=4.5).

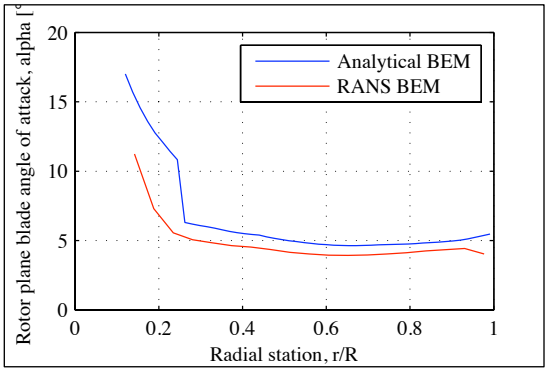

Figure 3.2.8: Illustration of the effects of blockage and ducting on blade angle of attack (λ=4.5).

The large differences in the integral rotor performance coefficients shown in Figure 3.2.5 and Figure 3.2.6 are indicators of significant differences to the blade local flow environment predicted by each technique. Figure 3.2.7 and Figure 3.2.8 illustrates the effect of blockage and ducting on the blade local axial flow velocity and local angle of attack for a rotor operating at a tip-speed-ratio of λ=4.5. Here, the combined effect of blockage and ducting is shown to reduce the axial flow velocity by ~10%. This leads to a delay in blade stall on the inboard radial sections for the RANS-BEM solution, leading to the shift in maximum C_p to a lower tip-speed-ratio, as shown in Figure 3.2.5. Blade stall inboard of the ~25% *r/R* radial station in the analytical simulation (Figure 3.2.8) results in higher flow rates through the center of the turbine, almost recovering free-stream velocities

close to the hub. Towards the outer radial stations a reduction in axial flow velocity for the RANS-BEM case is shown; attributed to the interaction of the rotor tips with boundary layer grown on the inner surface of the duct. An increase in velocity is shown for the analytical case; here attributed to the absence of a tip-loss model for the analytical case presented*, permitting higher axial velocities than would be seen under normal operating conditions for the baseline rotor.

In summary, it is shown that strong fluid-dynamic interactions, such as the blocked / ducted case studied here, are responsible for large departures from the unbounded uniform inflow results generated by analytical BEM techniques. Embedding a BEM solution within a RANS solver is potentially capable of addressing these interactions whilst retaining the advantages of a computationally light solution. This claim is later verified in Section 4.4, where good agreement is achieved between results of RANS-BEM and blade-resolved simulations†.

3.2.2 Embedded RANS Blade Element Method Design Tool

The design method presented here extends the capabilities of the standard RANS-BEM prediction method detailed in Section 3.1 to allow the iterative design of a tidal rotor operating *in-situ*. The design method is centred on the idea of achieving a target uniform local thrust coefficient,

$$c_x = \frac{F_x}{\frac{1}{2}\rho \Delta A u^2} \tag{3.1}$$

at a blade angle of attack consistent with the maximum lift to drag ratio of the local blade section used and a user specified tip-speed-ratio. Once initiated, the

* The tip-loss model is disabled for all ducted flow simulations. An assumption later verified in Section 4.4 of this report.

† RANS-computed aerofoil data is used as input to the RANS-BEM method.

design method iteratively adjusts blade chord, to influence local stream-wise loading, and blade twist, to modify the local angle of attack, as the solution progresses.

Betz shows that, for an unbounded rotor, optimal power performance is coincident with a stream-wise rotor thrust coefficient of

$$C_x = \frac{F_x}{\frac{1}{2}\rho \Delta A U_\infty^2} = \frac{8}{9}, \tag{3.2}$$

resulting in an optimum target local thrust coefficient of $c_x = 2$, as defined in Eq. (3.1). For solutions containing multi-body viscous interactions, the evaluation of optimum local disk loading is far less straightforward. Here, an iterative technique is employed. First, turbine designs for a number of coarsely spaced local disk loadings are made, creating a simple one-dimensional design space, as shown in Figure 3.2.9 for the blocked ducted case under study. A cubic interpolant is then fit (red line) through the initial trails (blue circles) to better estimate the optimum stream-wise loading. This estimate, $c_x = 1.1$ for the ducted case, is then run through the design tool once more producing an optimal power coefficient, based on disk area, of $c_p = 0.37$ (black cross).

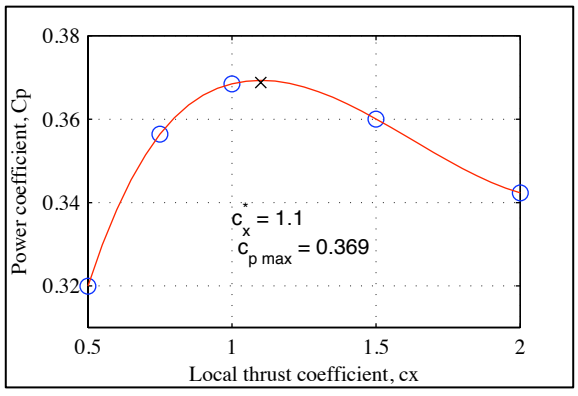

Figure 3.2.9: Illustration of the dependence of local thrust coefficient on rotor performance. Blue circles: initial trials; red line: cubic interpolant; black cross: final design.

Situations do arise, especially close to the rotor hub, where iterations towards a high target axial loading lead to significant blade overlap, indicated by local

solidity exceeding unity

$$\sigma = \frac{Nc}{2\pi r} < 1\,. \tag{3.3}$$

For these cases the target local blade angle of attack is first incrementally increased from the optimum lift-to-drag value α_{LD} up to a value corresponding to ether the maximum achievable blade torque coefficient

$$c_{\tau blade} = Cl\sin(\phi) - Cd\cos(\phi \tag{3.4}$$

or the maximum achievable blade thrust coefficient

$$c_{xblade} = Cl\cos(\phi) + Cd\sin(\phi \tag{3.5}$$

defined here as $\alpha_{\max}$. An illustrative example of this target angle of attack selection strategy is given in Figure 3.2.10 for the Goettingen 804 aerofoil section. Solidity and angle of attack limits are set to $\sigma = 1.25$ (accommodating slight blade overlap close to the hub) and $\alpha = \alpha_{\max}$ respectively. Once these limits are met, axial loading can no longer be increased. This results in an underachievement in axial thrust for the radial sections in question.

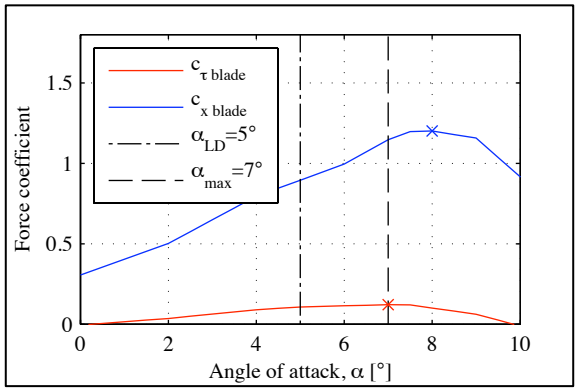

Figure 3.2.10: An illustrative example of acceptable target blade angle of attacks ranging from optimum lift-to-drag to the first maximum in ether torque or thrust coefficient for a solidity limited radial section (Goe804, Re 30,000, $\phi = 10°$).

3.2.3 RANS-BEM Rotor Designs

A number of design cases are now presented to illustrate the capabilities of the RANS-BEM design tool detailed above in Section 3.2.2. The rotors tested, listed in Table 3.2.1, comprise the UoM rotor along with RANS-BEM designs for unducted and ducted operation.

Label	Description
Rotor I	UoM rotor
Rotor II	Rotor designed for unducted operation within the EDF flume using RANS-BEM design tool.
Rotor III	Rotor designed for operation within duct H and the EDF flume using RANS-BEM design tool.

Table 3.2.1: Description of rotor designs.

Firstly, an alternate design to the UoM rotor (rotor I) is made* for a rotor operating in a blocked but unducted configuration (rotor II). Next, a design for a blocked rotor operating within duct H is presented (rotor III), with comparisons† to the rotor I operating in the same configuration. Finally, rotors II and III are compared for operation within duct H and the EDF flume. These case studies illustrate the advantages of a fully coupled (embedded) tidal turbine design tool.

Figure 3.2.11 illustrates a comparison between the power performance of rotors I and II operating in an unducted configuration within the EDF flume. Whilst the overall shape of the power coefficient curve remains the same

* As the UoM rotor was designed based on arguments of thrust matching to a larger scale design (WG4 WP2 D2) the comparisons that follow are made to illustrate the ability of the design tool at achieving an optimum power performance, using the UoM rotor as a baseline reference, rather than being presented as an alternate design.

† A flow blockage of b = 5% (Figure 2.3.1) is maintained for both ducted and unducted configurations.

between the two rotors, rotor II displays an appreciable increase in maximum power coefficient of ~12%. Figure 3.2.12 illustrates the corresponding comparison of overall thrust coefficient. Whilst the overall shapes are again similar, a higher thrust value for rotor II results.

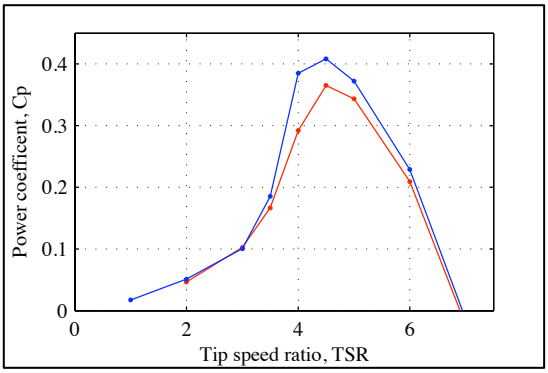

Figure 3.2.11: An illustrative comparison of power performance for rotors I and II (unducted).

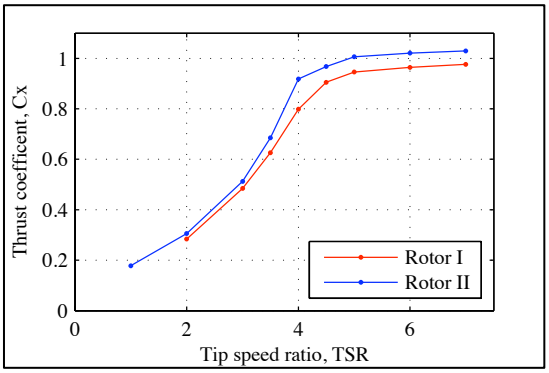

Figure 3.2.12: An illustrative comparison of thrust performance for rotors I and II (unducted).

Figure 3.2.13 illustrates the comparison of rotor power performance for the ducted baseline rotor (UoM) and a design-tool generated ducted rotor both operating within the EDF flume. An increase in maximum power coefficient of ~14% over the baseline design is achieved. This increase is accompanied by similar reductions in overall rotor thrust coefficient, again indicating an increase in basin efficiency for the bespoke rotor design, shown in Figure 3.2.14. A sharp decrease in power coefficient is shown in Figure 3.2.13 at low tip-speed-ratios. The absence of a helical vortex wake, modelled here by disabling the tip-loss model, results in an increase in stream-wise flow speeds across the outer blade stations. This in turn results in higher blade local angles of attack being maintained across the outer radial stations. As tip-speed-ratio is reduced, the gentle blade stall associated with a helical vortex wake is replaced with a sudden stall across the outer blade stations, leading to the sharp drop in power observed in Figure 3.2.13.

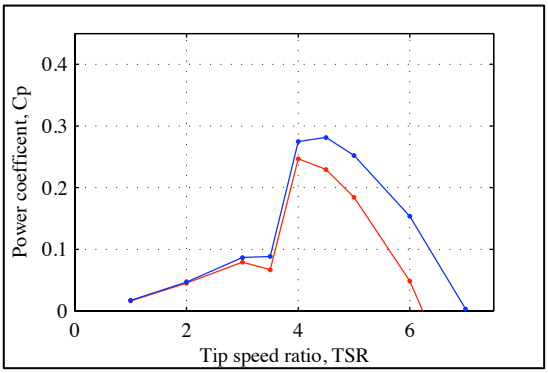

Figure 3.2.13: An illustrative comparison of power performance for rotors I and III (duct H)

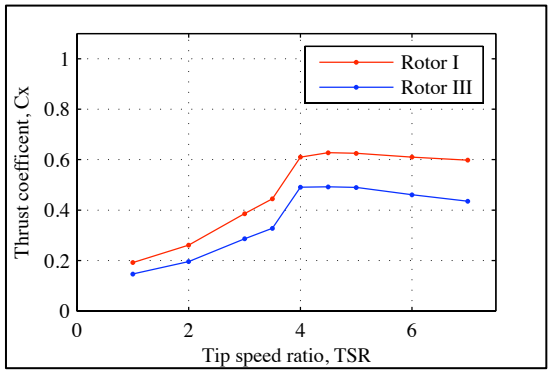

Figure 3.2.14: An illustrative comparison of power performance for rotors I and III (duct H).

Increases in maximum power coefficient of 12% and 14% are achieved by rotors II and III, with reference to rotor I, for unducted and ducted operation respectively. In order to isolate the influence of the baseline rotor geometry (rotor I) from that of the embedded RANS-BEM design tool, a comparison is now made between rotors II and III operating within duct H. Figure 3.2.15 illustrates a substantial increase in power coefficient of ~17%, showing both the effectiveness of the embedded design-tool and the importance of flow-field interactions for tidal turbine design. Once again, Figure 3.2.16 illustrates a lower overall rotor thrust coefficient generated by the rotor designed for purpose (operation within duct H).

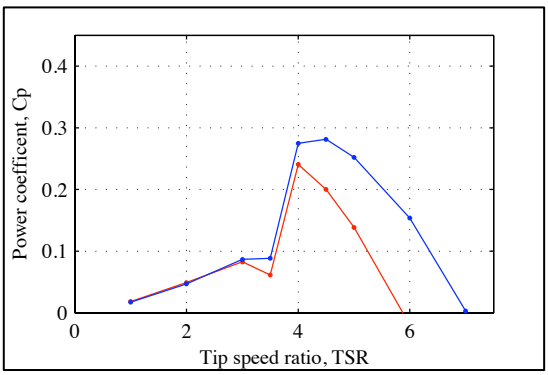

Figure 3.2.15: An illustrative comparison of power performance for rotors II and III (duct H).

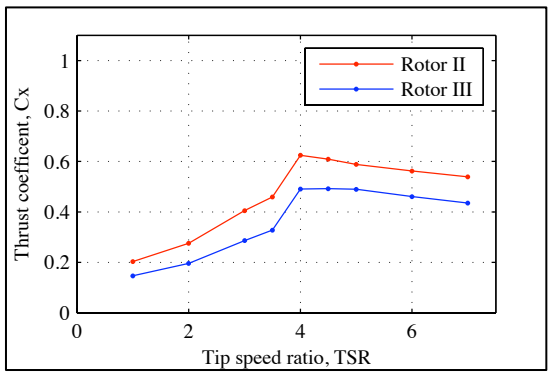

Figure 3.2.16: An illustrative comparison of thrust performance for rotors II and III (duct H).

Examination of local disk loading and angle of attack in Figure 3.2.19 and

Figure 3.2.20 for the two designs operating at a tip-speed-ratio of $\lambda = 4.5$ illustrates the influence of duct H on rotor operation. Whilst the rotor designed for a uniform disk loading of $c_x = 1.1$ (rotor III) achieves the optimal target thrust, the rotor designed for unducted operation (rotor II) displays a far greater local stream-wise loading increasing to a value approaching $c_x = 6$ close to the tips (likely to be a combination of the absence of a tip loss model for ducted flows and local flow acceleration due to the influence of the duct itself). Figure 3.2.20 shows the achievement of the target blade local angle of attack for all radial stations of $\alpha = \alpha_{LD} = 5°$ by the rotor designed for ducted flow (a requirement for optimal blade aerodynamic efficiency). The rotor designed for unducted flow however shows a wildly varying blade local angle of attack resulting in far greater blade aerodynamic losses, a contributing factor to the poor power performance and associated high overall stream-wise thrust coefficient reported.

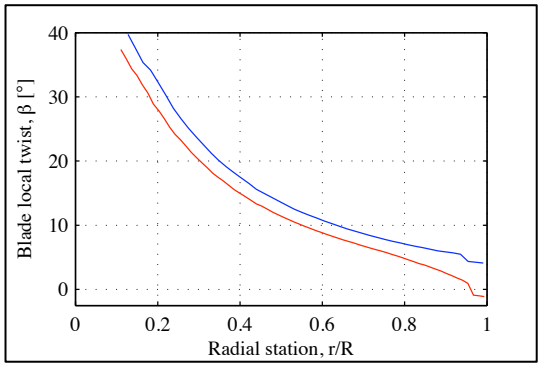

Figure 3.2.17: An illustrative comparison of blade twist for rotors II and III.

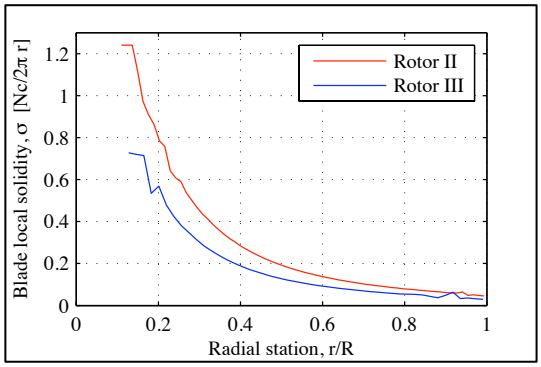

Figure 3.2.18: An illustrative comparison of local solidity for rotors II and III.

This section concludes with a comparison of rotors II and III. Blade twist is shown in Figure 3.2.17 to be $\sim 3°$ greater for the rotor designed for ducted operation. Differences in blade twist are seen to increase towards the tips. Here, rotor II, designed to accommodate the detrimental effects of tip loss, exhibits tip wash-out, which is absent in the rotor III design. Figure 3.2.18 shows a comparison of local solidity for the two rotor designs. Here, rotor III displays a much lower solidity than rotor II. As with blade twist, this difference is shown to

be a strong function of radial station.

The development and use of the embedded RANS-BEM design-tool has illustrated the importance of the inclusion of the combined effects of both blockage and ducting within any tidal turbine performance prediction method. Strong flow-field couplings should be considered primary drivers for tidal turbine designs and cannot be dismissed as secondary features.

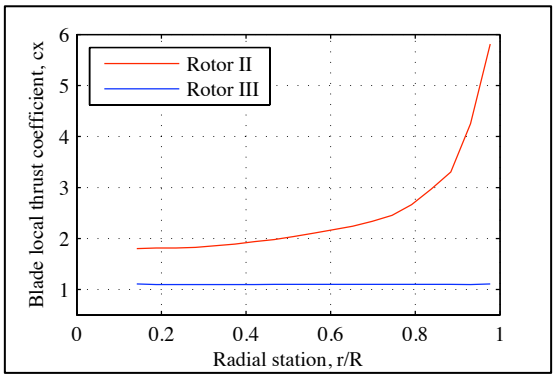

Figure 3.2.19: An illustrative comparison of blade local thrust coefficient for rotors II and III.

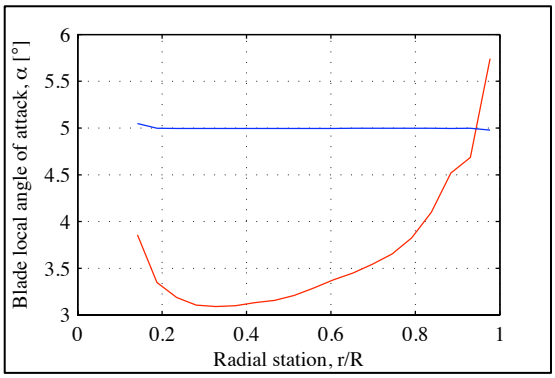

Figure 3.2.20: An illustrative comparison of blade local angle of attack for rotors II and III.

4 Blade-resolved Simulation

A series of three-dimensional RANS simulations of a ducted tidal turbine are presented in this section. The device is based on the 27 cm rotor previously tested by the University of Manchester, and duct H, selected in Section 2. Details are given of the meshing strategy, including convergence tests to ensure appropriate resolution of the blade geometry, as well as the computational setup. Finally, a selection of results are presented, with comparisons to both the unducted device simulated in WG3 WP1 D1, and the RANS BEM predictions in Section 3.

4.1 Geometry

The EDF flume geometry is longer than that presented previously in Figure 2.1.4, with the inlet and outlet located five diameters upstream and ten diameters downstream of the rotor plane respectively. In order to minimise blockage, the depth has been increased to 1 m, matching the maximum operating depth of the experimental flume. The width remains unaltered at 1.5 m.

The preceding section has shown that a rotor should be designed specifically for a particular duct. However, as this composite simulation is at the proof-of-concept stage the 27 cm UoM rotor from WG4 WP2 D2 is modelled. A computer-generated model of this rotor has been provided by the consortium. This rotor features rounded blade tips, which reduce losses in unducted operation. If the duct fits closely around the rotor, losses associated with a sharp tip geometry can be suppressed via a reduction in span-wise flows in these regions. Hence, it is appropriate to modify the rotor so that it has square tips, as illustrated in Figure 4.4.1. This requirement, in addition to the duct-rotor interactions highlighted in Section 3.2, may necessitate a new or modified design. The candidate rotor and duct designs contained within this report will be presented to the consortium to be considered for use within the experimental programme.

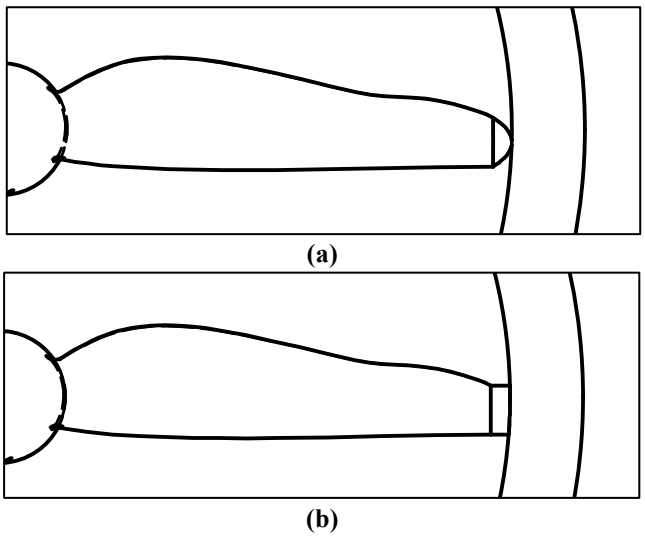

Figure 4.1.1: Illustration of modification to rotor tip showing (a) the original rotor, and (b) the modified rotor.

The hub geometry is based on the dynamometer used for some of the array-scale testing by UoM, with details given in Appendix D of WG4 WP2 D2. The duct for this device has been designed in Section 2. Dimensions of the best candidate design, duct H, are given in Figure 2.1.1(h). That design features a 35 cm rotor, while the rotor in this instance has a diameter of only 27 cm. A linear scaling factor of $^{27}/_{35}$ has been applied to produce the duct for the present simulations.

No support structure has been modelled, as it has not yet been designed by the consortium, and there are many possible configurations. The incorporation of a support structure into the present model will not pose any great difficulties. The rotating mesh region would be reduced to envelop the rotor only, with the hub, duct and associated support structure remaining in the stationary mesh region.

4.2 Meshing Strategy

Cell dimensions and boundary conditions largely correspond to those used in the composite simulations of the bare rotor operating within the EDF flume as detailed in WG3 WP1 D1.

4.2.1 Rotor Blades

A convergence study has been carried out on the rotor blade section to determine appropriate grid resolution for each rotor blade. Flow conditions at the 80% radius of the rotor for this case correspond to a Reynolds number of ~17,000. Within the PerAWaT consortium, experimental data for the aerofoil section used (Goettingen 804) is available for Reynolds numbers of 20,000 (Miley, 1982) and 30,000 (Hassan, 1993), with the former of the two datasets considered to be less reliable. While the Goettingen 804 section has a thin trailing edge, the rotor as provided by the consortium has a trailing edge thickness of 5% chord. In order to improve the likelihood of agreement with experimental data, this convergence study is carried out on a Goettingen 804 section with a thin trailing edge at $Re = 30{,}000$. For purposes of robust mesh generation, the thin trailing edge modelled has an actual thickness of 0.5% chord.

The forces on the blade are found to be very sensitive to boundary layer resolution, so the grids are modified on this basis. Far field resolution is based upon the high-resolution grid from WG3 WP1 D1. Surface elements have a maximum dimension of $0.2c$ on the upper and lower surfaces, where c is the chord length. The maximum surface element dimensions at the leading and trailing edges are $0.0025c$ and $0.005c$ respectively. The boundary layer is resolved by a number of layers of high aspect ratio prismatic elements. The first cell height is set to $0.0007c$, achieving a y^+ value of ~1.0, and a growth ratio of 1.2 is used. Details of three grids are given in Table 4.2.1, each with a different number of layers of prismatic elements.

Resolution	Node Count	Cell Count	Number of Layers of Prismatic Elements
Coarse	66938	222753	8
Medium	74331	230850	10
Fine	82049	229555	12

Table 4.2.1: Details of grids used in blade convergence study.

The aerofoil section is simulated for a range of angles of attack from -5° to 12° using the three grids listed above. Figure 4.2.1(a) shows consistent convergence of the drag polar with increasing boundary layer resolution. In Figure 4.2.1(b), convergence of lift-to-drag ratio at a 5° angle of attack is demonstrated. There is a difference of 12.2% between the coarse and medium grids, which is reduced to 4.0% between the medium and fine grids.

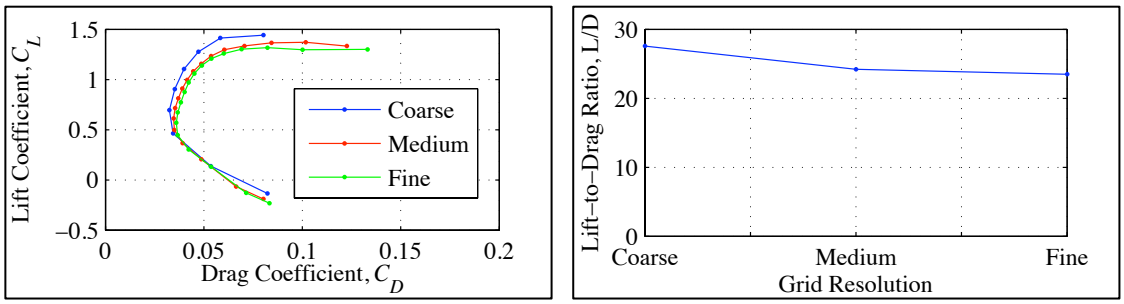

(a) **(b)**

Figure 4.2.1: Demonstration of grid convergence illustrating (a) the full drag polar (-5° < α < 12°) and (b) lift-to-drag ratio (α = 5°) across three levels of mesh refinement at Re = 30,000.

Considering the uncertainties associated with experimental data at this Reynolds number range, reasonably good agreement is achieved between the calculated and experimental drag polars (Figure 4.2.2).

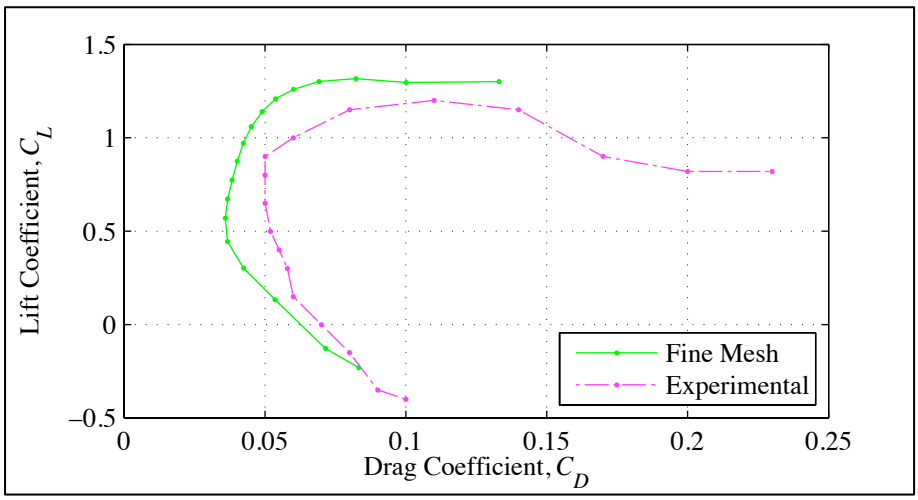

Figure 4.2.2: Comparison of calculated and experimental (Hassan, 1993) drag polars (unit span Goe-804; Re = 30,000; -5° < α < 12°).

Figure 4.2.3 highlights the influence of trailing edge thickness on computed drag polars. Increasing trailing edge thickness from 0.5% to 5% results in a minor shift of the polar to higher drag values.

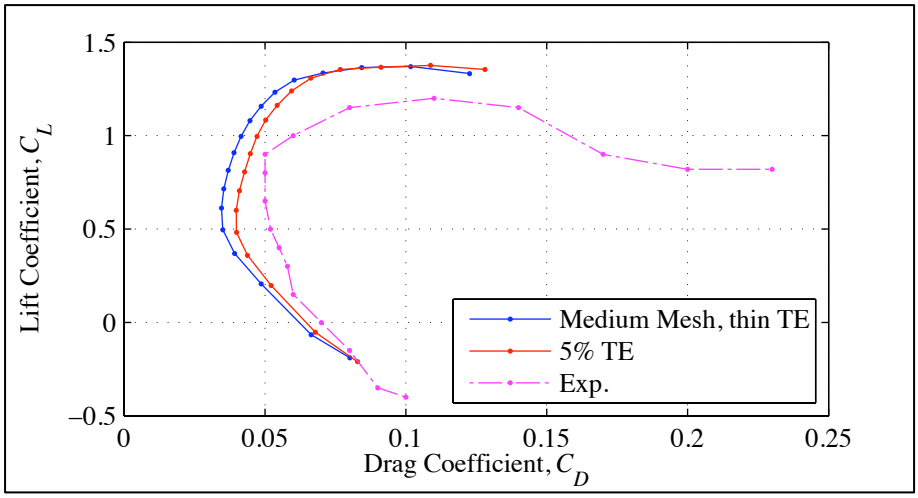

Figure 4.2.3: Effect of trailing edge thickness on drag polar, with experimental data shown for reference (Re = 30,000; -5° < α < 12°).

The aerofoil sections from Figure 4.2.3 have also been tested at a Reynolds number of 20,000, and the resulting drag polars are presented in Figure 4.2.4. While the experimental data at Re = 20,000 differs considerably from that at Re = 30,000, there is little difference between the respective computed results.

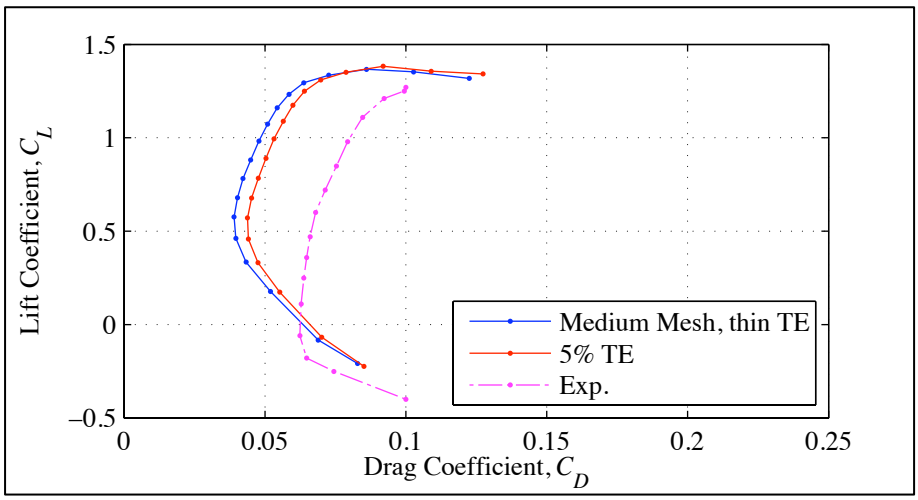

Figure 4.2.4: Thin trailing edge and 5% trailing edge sections, compared with experimental data (Re = 20,000; -5° < α < 12°).

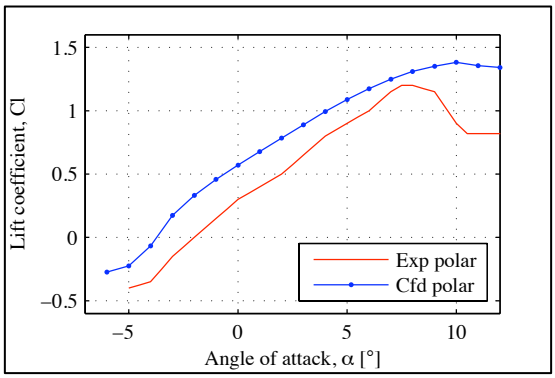

Figure 4.2.5: A comparison of experimental and computational lift coefficients (Goettingen 804, Re = 20,000).

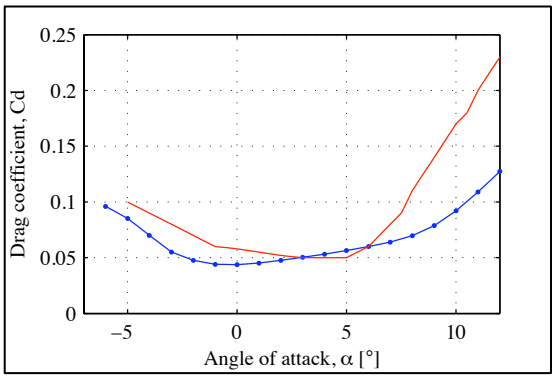

Figure 4.2.6: A comparison of experimental and computational drag coefficients (Goettingen 804, Re = 20,000).

Figure 4.2.5 and Figure 4.2.6 present comparisons between experimental and computational lift and drag data, plotted against angle of attack. Figure 4.2.5 illustrates that a far softer stall is predicted by the computational results. This is due to variations in stall mechanism brought about by the assumption of a 'fully turbulent' boundary layer in the computational model. Implications of this soft computational stall upon rotor performance are discussed further in Section 4.4.

Based on the results of this convergence study, cell dimensions on the rotor are specified according to the medium-resolution grid. Specifically, ten prismatic

boundary layers are used, with the wall-adjacent cell height set to achieve a y^+ value of 1.0 and a growth factor of 1.2. Maximum cell dimensions on the rotor surface, leading edge and trailing edge are set at $0.12c$, $0.0025c$, and $0.005c$ respectively, where c is the chord length at 80% blade radius. An illustration of mesh resolution on the rotor surface is presented in Figure 4.2.7.

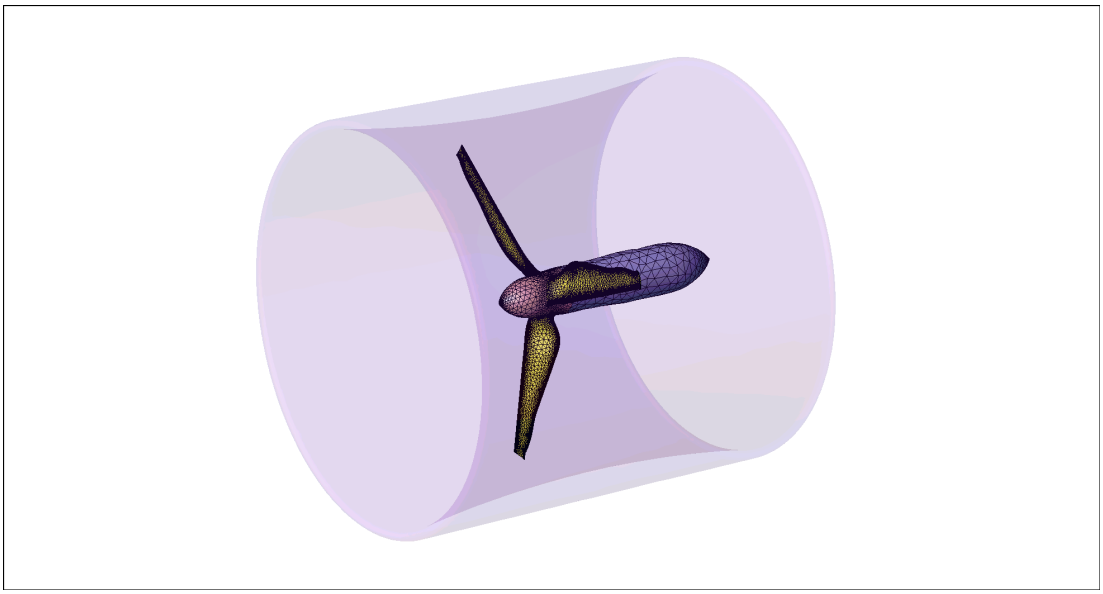

Figure 4.2.7: Illustration of mesh resolution on the rotor and hub, and the location of those bodies within the duct.

4.2.2 Flume, Duct and Hub

The CFD solver features a built-in logarithmic wall function, which can model the sheared velocity profile within a turbulent boundary layer. This model is activated when the y^+ value at the wall is greater than about 12.0, and is most effective in the range $30 < y^+ < 100$. The boundary layer is resolved at the walls and floor of the flume by four layers of prismatic elements with a wall y^+ of 100 and a growth factor of 1.2.

Surface element sizes on the duct and hub have been determined by the grid resolution study in Section 2.1.5. The boundary layer is explicitly resolved by ten layers of prismatic elements with a wall y^+ of ~1.0 and a growth factor of 1.2.

The entire ducted turbine is enclosed within a barrel-shaped rotating mesh region, visible in Figure 4.2.8.

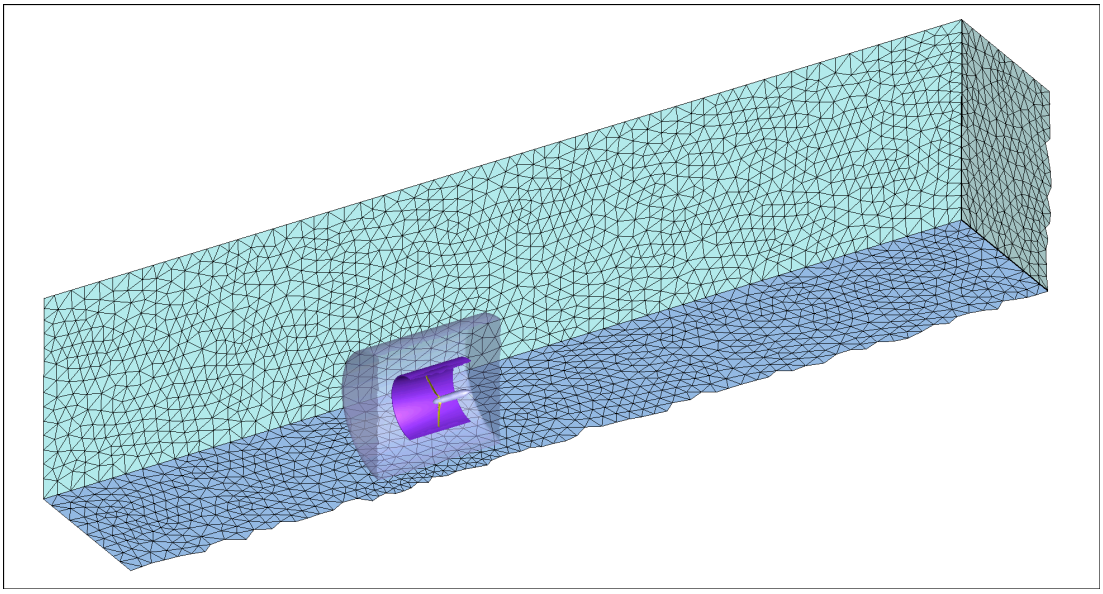

Figure 4.2.8: Cutaway view of computational model, showing the ducted turbine within a rotating mesh region.

4.3 Computational Model

A no-slip wall boundary condition is specified at the floor and sidewalls of the flume. A roughness height z_o = 3.21×10^{-6} has been calculated in WG3 WP1 D1, based on experimental data from the EDF flume (WG4 WP1 D3).

The development and validation of the free-surface model was reported in WG3 WP1 D1. In the interests of computational expedience, we choose, for the demonstrative solutions presented here, to use a rigid lid model in place of the free-surface model. The errors introduced by this approximation will be slight due to the relatively low blockage ratio. Significant blockage is required to achieve substantial difference between rigid lid and adaptive free-surface simulation results; 25% blockage yields a 1% change in power coefficient (Consul et al, 2011), whereas the blockage in the present simulations is 8.4%.

Angular motion of the rotor is achieved through the use of a barrel-shaped dynamic mesh region, which encompasses the rotor, hub and duct, and is illustrated in Figure 4.2.8. The device is simulated in operation at tip-speed ratios of 3.5, 4.0 and 4.5 by specifying angular velocities of 7, 8 and 9 *rad s*$^{-1}$ respectively in the rotating domain. A no-slip wall boundary condition, in the rotating reference frame, is applied at the rotor. No-slip wall boundary

conditions are also applied at the hub and duct surfaces. However, a rotational velocity of 0 $m\ s^{-1}$ is specified in the absolute frame of reference to prevent motion of those bodies.

Future simulations, which are to be compared with experiment, will feature sheared inflow velocity and turbulence profiles to match the flume environment. For the current demonstrative simulations, a uniform velocity of 0.27 $m\ s^{-1}$, a turbulence intensity of 0.1%* and a turbulent length scale of 0.1545 m are specified at the inlet. Solution stability is aided by ramping both the linear velocity at the inlet and the angular velocity of the rotor from zero to the target value over the first half-revolution.

The timestep sizes for each operating point, tabulated below, are based on the chord length at 80% radius, and the angular velocity of the rotor. Once the inflow and rotor velocities have ramped to their target values, each rotation is completed in approximately 375 timesteps.

Tip-speed Ratio	Angular Velocity [rad s^{-1}]	Timestep Size [s]
3.5	7	0.001862
4.0	8	0.002095
4.5	9	0.002394

Table 4.3.1: Timestep sizes for each operating point.

4.4 Flow Field Analysis

A history of the power coefficient over three revolutions is presented in Figure 4.4.1. The power coefficient is calculated as

* A low inflow turbulence intensity has been used here to aid comparison with the RANS BEM results. A demonstration of high turbulence intensity sheared inflow computations is given previously in WG3 WP1 D1.

$$C_P = \frac{\omega\tau}{\frac{1}{2}\rho A_{ref} u_\infty^3}, \tag{6}$$

where τ is the total torque on the rotor and spinner, and ω is angular velocity of the rotor. Unlike the corresponding results in WG3 WP4 D1, fluctuations associated with blade-tower interaction are not present due to the absence of any support structure.

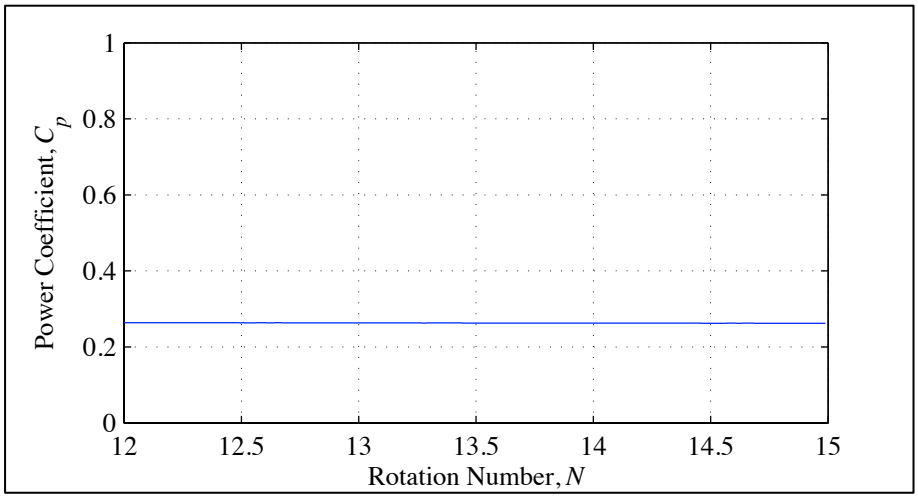

Figure 4.4.1: History of power coefficient for three rotations at a tip speed ratio of 4.0.

The total thrust on the rotor and spinner is plotted in coefficient form in Figure 4.4.2. A steady thrust history is observed.

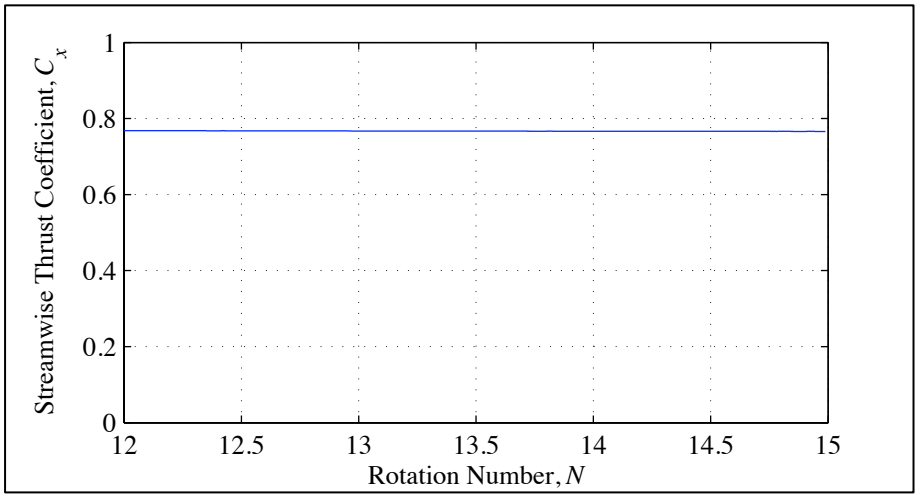

Figure 4.4.2: History of streamwise thrust coefficient for three rotations at a tip speed ratio of 4.0.

Contours of velocity magnitude at the horizontal midplane of the device are presented in Figure 4.4.3. Blockage effects are visible in the form of a low-velocity wake region surrounded by an accelerated bypass flow. Leading edge separation is indicated by the locally accelerated flow in that region.

One pertinent feature of the ducted turbine is that a helical tip-vortex structure, readily identifiable in unducted rotor wakes (Figure 4.4.4), is not discernible (Figure 4.4.3). This is attributed to a bounding effect of the inner duct wall. Here, bound circulation is maintained at the blade tip, thus limiting the production of a tip vortex. Vorticity responsible for flow retardation through the duct is instead shed from the trailing edge of the duct as a continuous sheet.

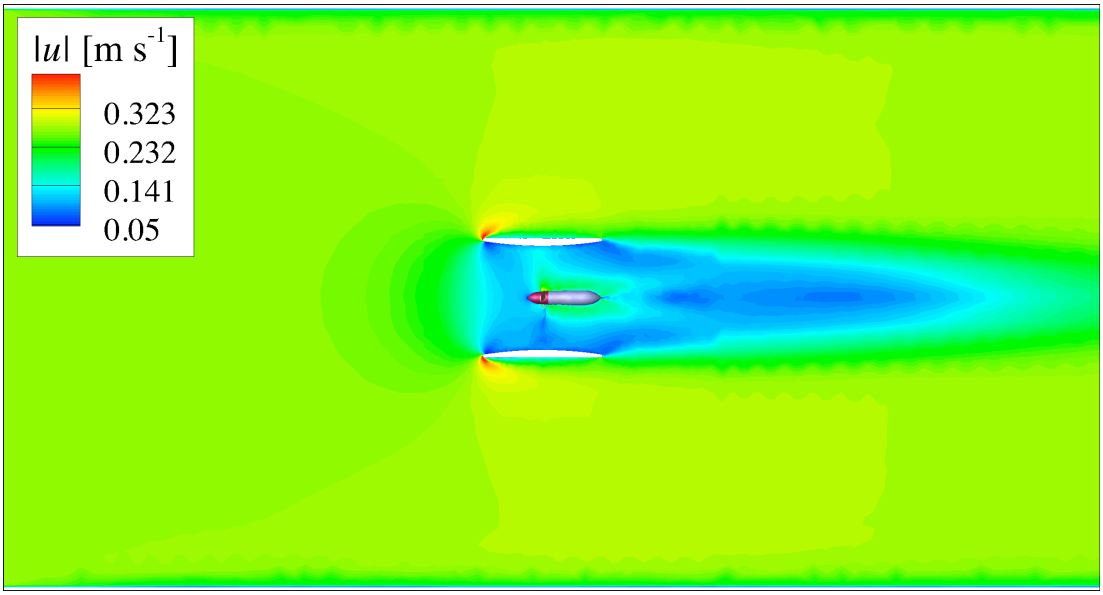

Figure 4.4.3: Instantaneous contours of velocity magnitude at the horizontal midplane of the device (λ = 4.0, U0, T0).

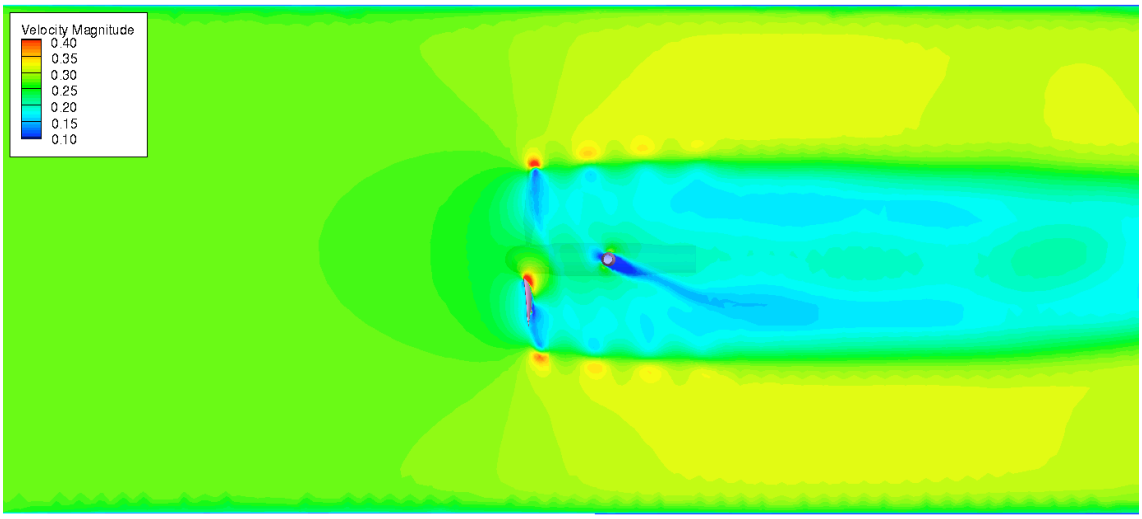

Figure 4.4.4: Instantaneous contours of velocity magnitude at a horizontal slice placed 1/3 of a radius above the flume centreline for the unducted case simulated in WG3 WP1 D1 (λ = 3.5, U0, T0).

Pressure contours on a series of vertical slices through the flow field are presented in Figure 4.4.5, Figure 4.4.6 and Figure 4.4.7. The local pressure jump that is visible across each blade is primarily responsible for the high streamwise thrust coefficient, and is necessary for power extraction by the turbine. Figure 4.4.8 shows the corresponding pressure field around the unducted device simulated in WG3 WP1 D1, where both tip and root vortices are visible. Tip vortices are not generated by the ducted device due to the presence of the duct. The distinct root vortices visible in Figure 4.4.8 are shed from the sharp corner of the trailing edge of each blade near its root where there is a marked reduction in blade chord and hence bound circulation.

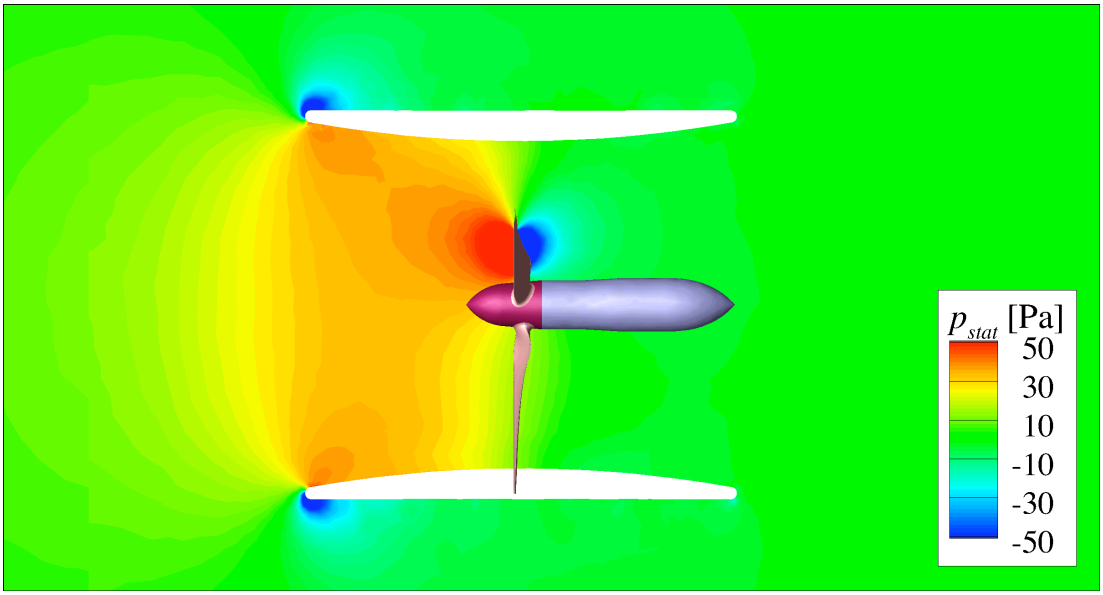

Figure 4.4.5: Instantaneous contours of static pressure at a vertical slice offset one half-radius beyond the device centreline.

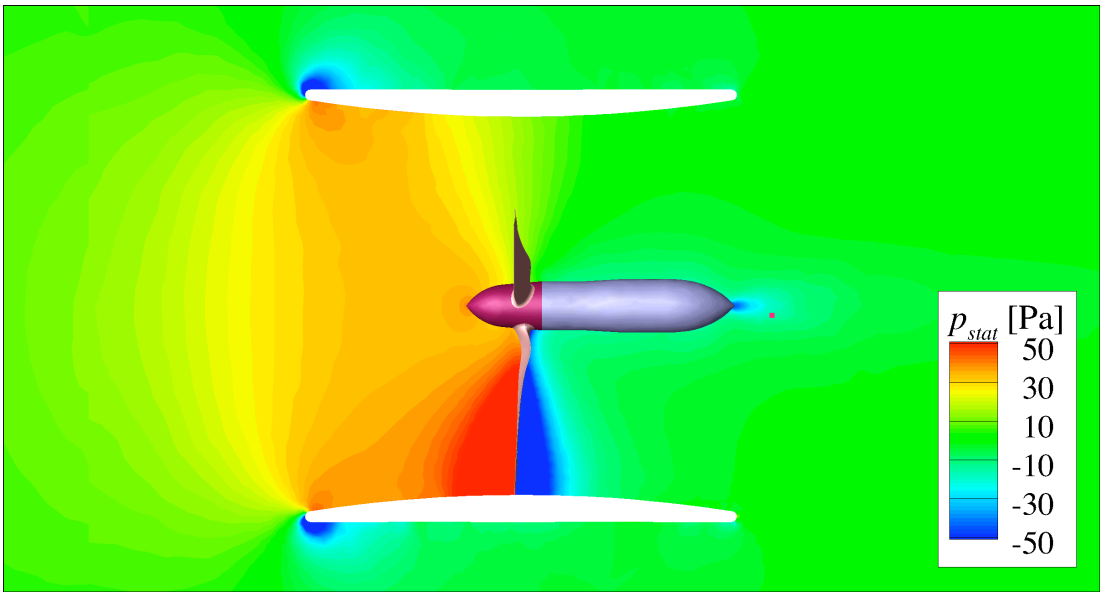

Figure 4.4.6: Instantaneous contours of static pressure at the vertical midplane of the device.

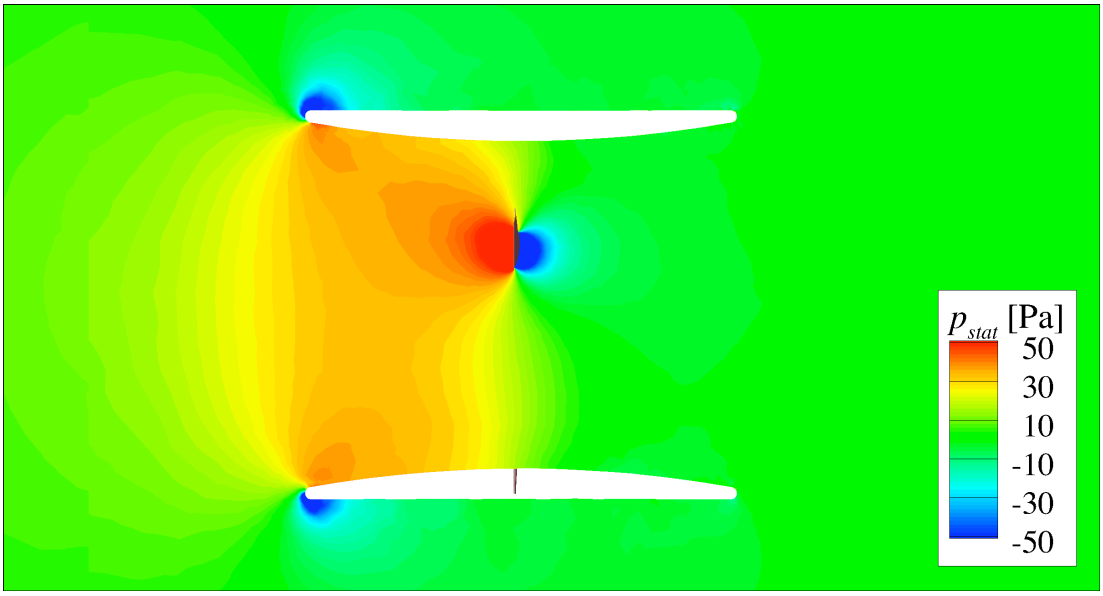

Figure 4.4.7: Instantaneous contours of static pressure at a vertical slice offset one half-radius ahead of the device centreline.

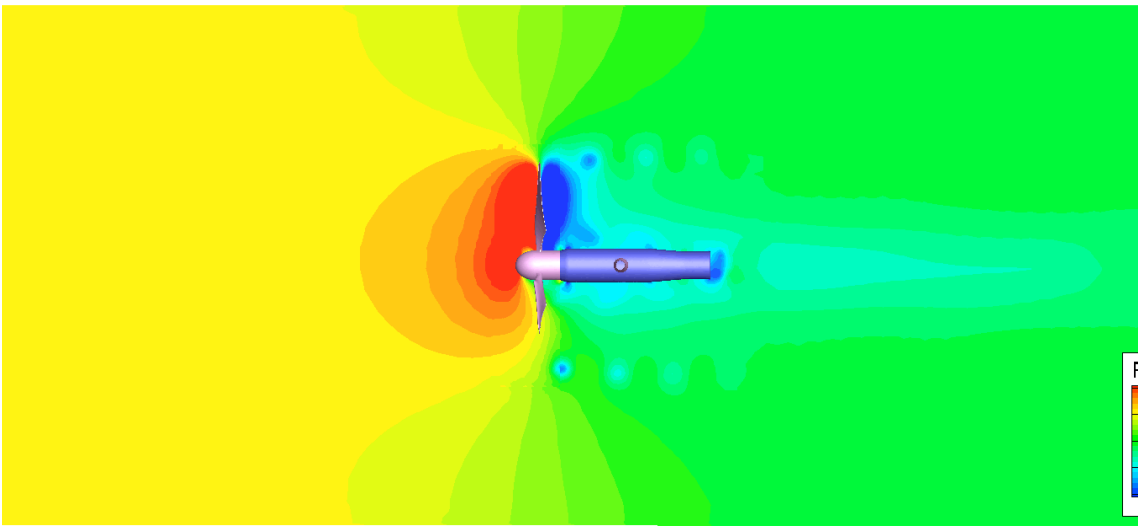

Figure 4.4.8: Instantaneous contours of static pressure at the vertical midplane of the unducted device simulated in WG3 WP1 D1.

An isometric view of the ducted device in operation is presented in Figure 4.4.9. The instantaneous velocity field is captured by a series of stream-tracers. The swirl imparted on the fluid by the rotor is visible downstream of the turbine. An iso-surface of vorticity has been generated and coloured by contours of static pressure. High-pressure regions are visible on the leading edge of the duct and

spinner, and the upstream surfaces of the blades.

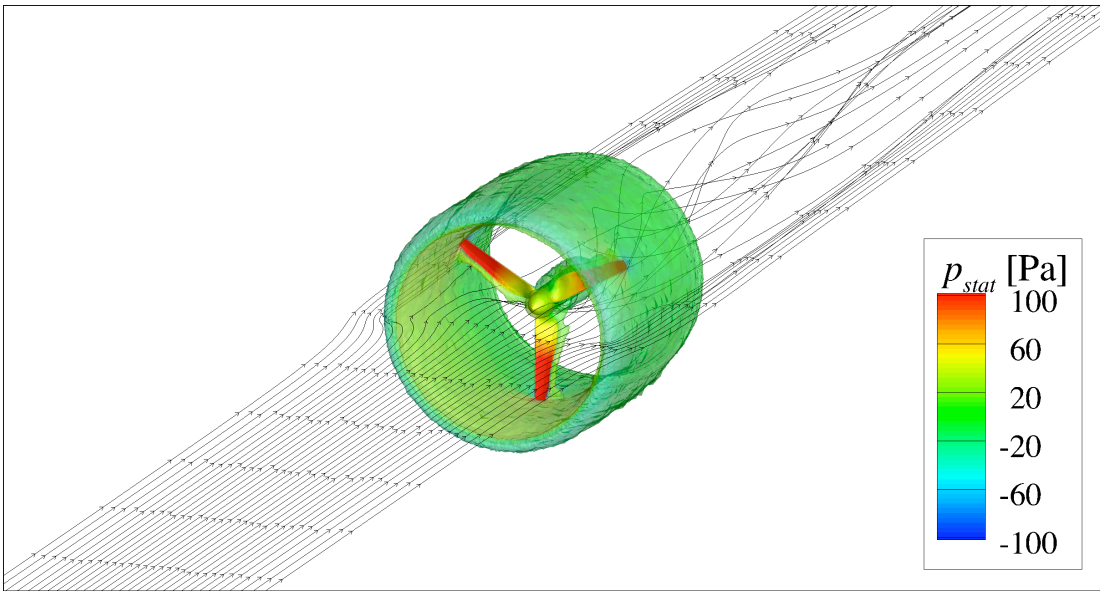

Figure 4.4.9: Isometric view of turbine with the instantaneous velocity field highlighted by stream-tracers along with iso-surface of vorticity coloured by static pressure.

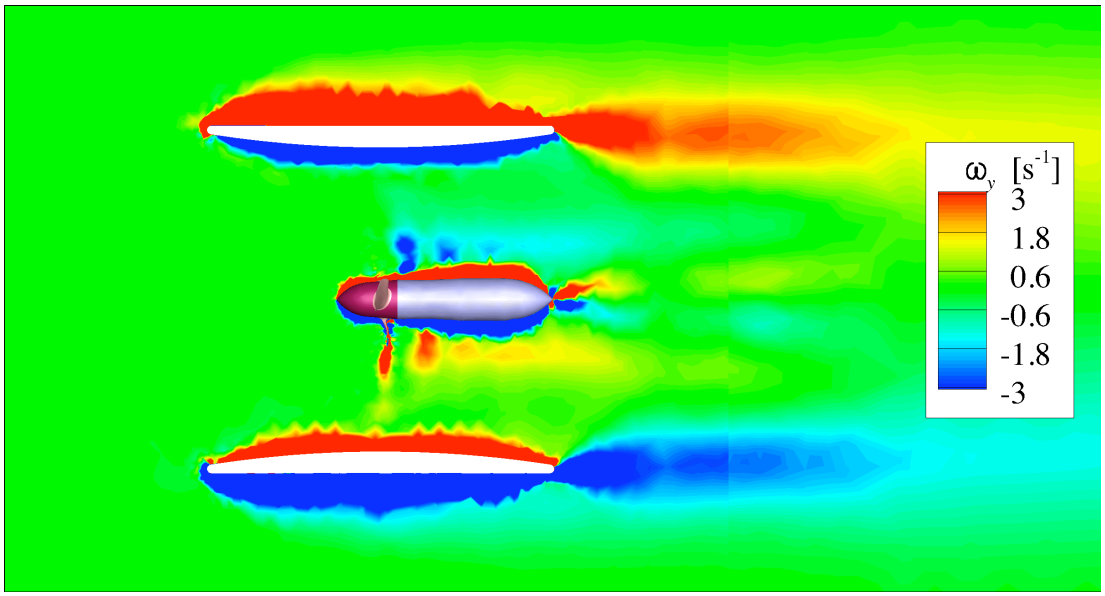

Figure 4.4.10: Contours of y-vorticity on the horizontal midplane of the device.

Root vortices shed from the trailing edges of the rotor blades are visible in Figure 4.4.10. A continuous sheet of vorticity emanating from the duct trailing edge is clearly visible, supporting claims concerning the influence of the duct on the suppression of a helical vortex wake.

RANS-BEM rotor performance predictions are shown for two distinct sets of

aerofoil input data. The first set is taken from wind tunnel experiments (Miley, 1982) with the second produced by computation (Figure 4.2.5 and Figure 4.2.6). Very good agreement for power performance is observed between RANS-BEM (computed polars) and blade-resolved simulations (Figure 4.4.11). A larger disagreement is seen in predictions of thrust performance (Figure 4.4.12). Underperformance in thrust prediction may be the result of differences between blade-resolved and RANS-BEM input geometries*. Largest close to the blade root, these geometrical differences influence thrust predictions (scaling with r^2) to a greater extent than predictions of rotor power (scaling with r^3).

RANS-BEM solutions employing the experimental aerofoil polar show a large disagreement with the blade-resolved simulations at a tip-speed-ratio of $\lambda = 3.5$. The source of this error is readily identifiable as a failing in computational force predictions for low Reynolds number aerofoil flows (Figure 4.2.5 and Figure 4.2.6). This is verified by the excellent agreement achieved using the computed polars (Figure 4.4.11). The RANS-BEM method employing experimental aerofoil polars circumvents this stumbling block and is thus presented as the solution method in which most confidence is placed.

* The rotor geometry for the blade-resolved simulations is based on CAD data provided by the consortium, whereas the rotor geometry for the RANS-BEM simulations is defined according to the tabulated data in WG4 WP2 D2 (Appendix F).

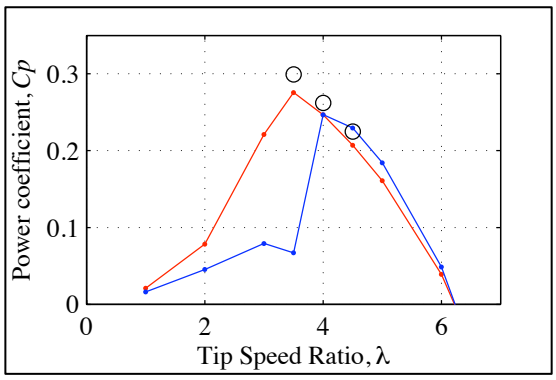

Figure 4.4.11: A comparison of power performance predictions by blade-resolved and RANS-BEM simulations.

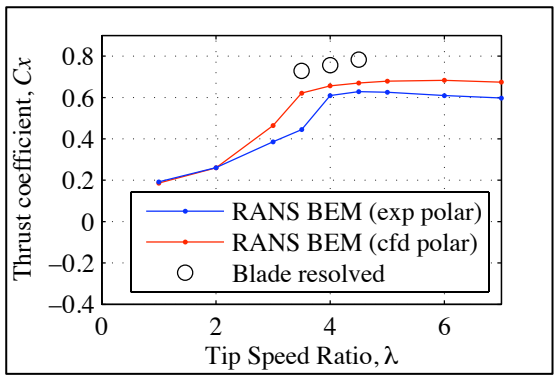

Figure 4.4.12: A comparison of thrust performance predictions by blade-resolved and RANS-BEM simulations.

A further justification of the RANS-BEM method is based on solution time. Typical data for required computational resource for the various simulation methods presented in this report are listed in Table 4.4.1.

Method	Cores	Hours (approx.)
Actuator Disk - unsteady	4	15
Actuator Disk - steady	4	2
RANS-BEM design	4	2
RANS-BEM simulation	4	2
Blade-resolved simulation	8	250

Table 4.4.1: Typical computational resource requirements for simulations presented in this report.

The computational overhead associated with blade-resolved simulations of a ducted tidal turbine for a single operating point (~2000 CPU hours) is about two orders of magnitude greater than that associated with BEM-RANS simulations (~8 CPU hours).

5 Conclusions

A bi-directional duct for a tidal turbine has been designed based on the results of a parametric computational study of ducted devices. Comparisons are made in an unconventional but fair manner, where performance coefficients are normalised on overall device cross-sectional area rather than on rotor area. The unducted device tested has a rotor diameter equal to the external diameter of the ducted devices. Hence, a ducted device must achieve a balance between increased mass flow rate and reduced rotor diameter. The best bi-directional ducted device achieves a maximum power coefficient of only 57% of that of an unducted device.

A computationally expedient method of rotor modelling, involving a combination of the widely-used BEM method and a commercial RANS flow solver, has been developed and validated. A power curve is produced for comparison to blade-resolved simulations. The method provides a tractable tool for rotor design in a constrained flow environment. The RANS-BEM method is used to make performance comparisons of ducted devices with rotors designed for unbounded and bounded flows, with the latter design generated using the present RANS-BEM code.

Finally, a series of blade-resolved simulations of the newly-designed ducted device are carried out. For moderate to high tip-speed-ratios good agreement is achieved between blade-resolved simulations and RANS-BEM simulations, where the underlying blade lift and drag data is generated numerically by the present RANS solver. Over this tip-speed-ratio range there appears no significant advantage of blade resolved simulation over RANS-BEM simulation. In fact, the computational cost of RANS-BEM simulations is found to be approximately two orders of magnitude less than blade-resolved simulations.

However, there are significant differences between the RANS-BEM solutions employing experimental and numerical lift and drag data. This underlines the limitations of RANS based solution strategies, be they blade-resolved or RANS-BEM with RANS computed blade data, for blades operating at low Reynolds

numbers. This is due to the inability of RANS based solvers to correctly predict transition and separation at low Reynolds numbers.

Examination of the flow field of the blade-resolved simulations reveals that no discrete tip vortices are shed from the rotor. Hence, the detrimental effect associated with vortex-induced tip losses, usually associated with rotor flow, is largely avoided.

6 References

ANSYS (2009). *ANSYS FLUENT 12.0 User's Guide*.

ANSYS (2010). *ANSYS ICEM CFD 13.0 User Manual.*

AECOM (2009). *Fundy Tidal Energy Demonstration Project, Volume II: Appendices, Appendix 2.* Available from http://www.gov.ns.ca/nse/ea/minas.passage.tidal.demonstration.asp, accessed January 2011.

BELLONI, C. & WILLDEN, R.H.J. (2010). *A computational study of a bi-directional ducted tidal turbine.* 3rd International Conference on Ocean Energy, Bilbao 2010.

BOSSANYI, E. A. (2003). *GH Bladed - Theory Manual.* Technical Report 282/BR/009. Garrad Hassan and Partners Ltd.

BURTON, T., SHARPE, D., JENKINS, N., BOSSANYI, E. (2001). *Wind Energy Handbook.* John Wiley & Sons Ltd.

CLEAN CURRENT LTD. www.cleancurrent.com (accessed January 2011).

CONSUL, C.A., WILLDEN, R.H.J., MCINTOSH, S.C. (2011). *An Investigation of the Infulence of Free Surface Effects on the Hydrodynamic Performance of Marine Cross-Flow Turbines.* European Wave and Tidal Energy Conference 2011, University of Southampton.

GRASSMANN, H., BET, F., CABRAS, G., CESHIA, M., COBAI, D., DELPAPA, C. (2003). *A Partially Static Turbine - First Experimental Results.* Technical Note, Renewable Energy 28, 1779-1785.

HANSEN, M. O. L., (2008). *Aerodynamics of Wind Turbines.* James & James Ltd.

HANSEN, M. O. L., SØRENSEN, N. N., FLAY, R. G. J., (2000). *Effect of Placing a Diffusert around a Wind Turbine.* Wind Energy; **3**:207-213.

HASSAN, U., (1993). *A Wind Tunnel Investigation of the Wake Structure Within Small Wind Turbine Farms.* Technical Report ETSU WN 5113. Garrad Hassan and Partners Ltd.

MILEY, S.J., (1982). *A Catalog of Low Reynolds Number Airfoil Data for Wind Turbine Applications.* DE82-021712.NTIS.

OPENHYDRO LTD. www.openhydro.com (accessed January 2011).

SHIVES, M. AND CRAWFORD, C., (2010). *Overall Efficiency of Ducted Tidal Current Turbines.* OCEANS 2010, pp.1-6, 20-23 Sept. 2010.

VITERNA, L. A., CORRIGAN, R. D. (1981). *Fixed Pitch Rotor Performance of Large Horizontal Axis Wind Turbines.* DOE/NASA Workshop on Large Horizontal Axis Wind Turbines, Cleveland, Ohio, USA, 1981; 69 - 85.